Monthly Notices
of the
ROYAL ASTRONOMICAL SOCIETY

MNRAS **483,** 4586–4614 (2019)
Advance Access publication 2018 December 19

doi:10.1093/mnras/sty3449

Cold molecular outflows in the local Universe and their feedback effect on galaxies

A. Fluetsch,[1,2]★ R. Maiolino,[1,2] S. Carniani,[1,2] A. Marconi,[3,4] C. Cicone,[5] M. A. Bourne,[2,6] T. Costa,[7] A. C. Fabian,[6] W. Ishibashi[6] and G. Venturi[1,2,3,4]

[1]*University of Cambridge, Cavendish Laboratory, Cambridge CB3 0HE, UK*
[2]*University of Cambridge, Kavli Institute for Cosmology, Cambridge CB3 0HE, UK*
[3]*Dipartimento di Fisica e Astronomia, Universitá degli Studi di Firenze, 50019 Firenze, Italy*
[4]*INAF Osservatorio Astrofisico di Arcetri, 50125 Firenze, Italy*
[5]*INAF Osservatorio Astronomico di Brera, Via Brera 28, I-20121 Milano, Italy*
[6]*Institute of Astronomy, Madingley Road, Cambridge CB3 0HA, UK*
[7]*Leiden Observatory, Leiden University, PO Box 9513, NL-2300 RA Leiden, the Netherlands*

Accepted 2018 December 7. Received 2018 December 6; in original form 2018 May 11

ABSTRACT

We study molecular outflows in a sample of 45 local galaxies, both star forming and active galactic nucleus (AGN), primarily by using CO data from the Atacama Large Millimeter/submillimeter Array (ALMA) archive and from the literature. For a subsample, we also compare the molecular outflow with the ionized and neutral atomic phases. We infer an empirical analytical function relating the outflow rate simultaneously to the star formation rate (SFR), $L_{\rm AGN}$, and galaxy stellar mass; this relation is much tighter than the relations with the individual quantities. The outflow kinetic power shows a larger scatter than in previous, more biased studies, spanning from 0.1 to 5 per cent of $L_{\rm AGN}$, while the momentum rate ranges from 1 to 30 times $L_{\rm AGN}/c$, indicating that these outflows can be both energy driven, but with a broad range of coupling efficiencies with the interstellar medium (ISM), and radiation pressure driven. For about 10 per cent of the objects, the outflow energetics significantly exceed the maximum theoretical values; we interpret these as 'fossil outflows' resulting from activity of a past strong AGN, which has now faded. We estimate that, in the stellar mass range probed here ($> 10^{10}\,{\rm M}_{\odot}$), less than 5 per cent of the outflowing gas escapes the galaxy. The molecular gas depletion time associated with the outflow can be as short as a few million years in powerful AGN; however, the total gas (H_2 + H I) depletion times are much longer. Altogether, our findings suggest that even AGN-driven outflows might be relatively ineffective in clearing galaxies of their entire gas content, although they are likely capable of clearing and quenching the central region.

Key words: galaxies: active – galaxies: evolution – galaxies: ISM – quasars: general – galaxies: star formation.

1 INTRODUCTION

Galactic outflows driven either by active galactic nuclei (AGNs) or starbursts may be capable of expelling ionized, atomic neutral and molecular gas from galaxies and thereby regulate or even shut down star formation. As a consequence, outflows may provide the (negative) feedback effect that is invoked to explain several key observable properties of galaxies. For instance, star formation suppression from AGN-driven outflows is thought to play a key role in accounting for the local population of massive passive galaxies and the lack of overmassive galaxies (e.g. Scannapieco & Oh 2004; Springel, di Matteo & Hernquist 2005; Sijacki et al. 2007; Puchwein & Springel 2013; Vogelsberger et al. 2014; Beckmann et al. 2017). Furthermore, this process may offer an explanation for the tight correlations between the masses of the central supermassive black holes (SMBHs) and the stellar masses or velocity dispersions of their host galaxy bulges (e.g. Fabian 2012; King & Pounds 2015). On the other hand, starburst-driven outflows are thought to play a key role in self-regulating star formation in low-mass galaxies and also to be responsible for the chemical enrichment of the circumgalactic medium (e.g. Erb 2015; Chisholm et al. 2017).

★ E-mail: af618@mrao.cam.ac.uk

In the last few years, extensive observing programmes have been dedicated to the detection and characterization of galactic outflows, especially powerful outflows that are driven by AGN. Several studies have investigated the warm-ionized phase of outflows, finding velocities up to several 1000 km s^{-1} and radii up to several kpc (e.g. Westmoquette et al. 2012; Arribas et al. 2014; Harrison et al. 2014; Rupke, Gültekin & Veilleux 2017). In high-z quasars (QSOs) such ionized outflows are seen to spatially anticorrelate with star formation in the host galaxy, which has been regarded as direct evidence for quasar-driven outflows quenching star formation in galaxies (Cano-Diaz et al. 2012; Carniani et al. 2016, 2017). Numerous studies have confirmed the presence of prominent neutral atomic outflows in local galaxies (Morganti, Tadhunter & Oosterloo 2005; Rupke, Veilleux & Sanders 2005a; Cazzoli et al. 2016; Morganti et al. 2016; Rupke et al. 2017). However, among all the gas phases involved in galactic outflows, the molecular phase is of particular interest, because it is found to dominate the outflow mass (Feruglio et al. 2010; Rupke & Veilleux 2013; Cicone et al. 2014; Carniani et al. 2015; García-Burillo et al. 2015; Fiore et al. 2017). Furthermore, molecular gas is the phase out of which stars form; hence, molecular outflows directly affect star formation.

Molecular outflows have been detected through P-Cygni profiles of far-infrared (FIR) OH transitions (Fischer et al. 2010; Sturm 2011; Spoon et al. 2013; Veilleux et al. 2013; Stone et al. 2016; González-Alfonso et al. 2017) and through broad wings seen in interferometric observations of molecular transitions such as low-J CO lines (Feruglio et al. 2010; Cicone et al. 2012; Combes et al. 2013; Sakamoto et al. 2014; García-Burillo et al. 2015) as well as higher density tracers such as HCN (Aalto et al. 2012, 2015; Walter et al. 2017). Using CO line mapping, Cicone et al. (2014) found that starburst galaxies have outflow mass-loading factors [$\eta = \dot{M}_{\rm outf}({\rm H_2})/{\rm SFR}$] of 1–4, but the presence of an AGN dramatically increases η. Depletion time-scales due to the outflow, i.e. $\tau_{\rm dep,outf}({\rm H_2}) \equiv M({\rm H_2})/\dot{M}_{\rm outf}({\rm H_2})$, were found to anticorrelate with $L_{\rm AGN}$, which further indicates that AGN boost galactic outflows. In a study of AGN wind scaling relations including molecular and ionized winds, Fiore et al. (2017) observed that molecular outflow mass rates correlate with AGN luminosity as $\dot{M}_{\rm outf}(H_2) \propto L_{\rm AGN}^{0.76}$, while the ionized outflow mass rates has a steeper dependence of the form $\dot{M}_{\rm outf}({\rm ion}) \propto L_{\rm AGN}^{1.29}$, suggesting that at high luminosities the ionized phase may contribute significantly to the mass-loss rate. However, it should be noted that these results were achieved by comparing outflow phases observed in different samples of galaxies; hence, these results are potentially subject to (differential) selection effects among samples selected to investigate different phases.

The purpose of this work is not to provide a census of molecular outflows in galaxies (which would require high sensitivity millimetre data for a large, volume-limited or mass-limited sample of galaxies), but it is to explore the scaling relations between molecular outflows and galaxy properties. This will shed light on the driving mechanisms of outflows and their effect on the host galaxies. We improve relative to previous studies by significantly increasing the statistics with a sample size of nearly 50 galaxies (which is more than twice that of previous molecular outflow studies using CO data) and by tackling some of the biases and selection effects. We use interferometric CO measurements that allow us to determine the velocity and spatial extent of the outflows. We specifically investigate the relations between outflow and galaxy properties such as star formation rate (SFR), stellar mass, and AGN luminosity. Furthermore, we include data from the ionized and atomic phase of the outflow for those galaxies in our sample that have this information available, and we investigate their relationship with the molecular phase. This is crucial since galactic outflows are multiphase and by focussing only on one phase the total impact of galactic winds on the interstellar medium (ISM) might be underestimated (e.g. Cicone et al. 2018a).

Throughout this work, a $H_0 = 70\,{\rm km\,s^{-1}\,Mpc^{-1}}$, $\Omega_{\rm M} = 0.27$, and $\Omega_\Lambda = 0.73$ cosmology is adopted.

2 SAMPLE AND DATA ANALYSIS

2.1 Sample Selection

We have characterized molecular outflows by collecting data both from the literature and from an extensive analysis of Atacama Large Millimeter/submillimeter Array (ALMA) archival data. We set an upper limit of $z < 0.2$ on the redshifts of the targets, since beyond this redshift the angular resolution of most ALMA archival observations (>0.3 arcsec) probes scales too coarse (>1 kpc) to enable a proper characterization of outflows. We search the ALMA archive for low-J transitions [i.e. CO(1–0), CO(2–1) and CO(3–2)] of all local galaxies observed in these transitions and with publicly available data in the archive as of 2018 April 1. As a result, we have analysed about 100 galaxies from the ALMA archive. However, most of these data have turned out to have sensitivities too low to enable the detection of putative faint broad CO transitions associated with outflows. However, we have detected outflow signatures in seven of these galaxies, according to the procedure described in Section 2.2.

We generally do not use the ALMA observations for which there is no outflow detection to set upper limits on the outflow properties (e.g. outflow rate, kinetic power, and momentum rate), since these would need knowledge of both outflow size and velocity, which is not known a priori. Yet, we can infer tentative upper limits in three cases for which the outflow is detected in other phases (in particular the ionized phase) by assuming that the (undetected) molecular outflow has the same size and velocity as those observed in the detected outflow phases. As a consequence, from the ALMA archive we have obtained molecular outflow information for a total of 10 galaxies (7 detections and 3 upper limits).

For what concerns the literature sample, we have searched for published molecular outflows at $z < 0.2$ obtained through the analysis of the CO(1–0) and CO(2–1) emission lines. We have compiled a total of 31 galaxies with published molecular outflows (five of which are upper limits).

We also include four ULIRGs from González-Alfonso et al. (2017) in our sample. In these cases, the molecular outflow properties have been determined based on the FIR transitions of OH observed through the Herschel/PACS spectrometer. Their outflow mass rates are calculated assuming a single expulsion of gas, which is analogous to what we assume in this paper (as it will be described in Section 2.3). For an additional four galaxies of the González-Alfonso et al. (2017) sample, the molecular outflow rates inferred from OH have been measured also through CO observation and in these cases they are in reasonable agreement (typically within a factor of 2).

The total sample used in this work consists of 45 galaxies whose properties, such as redshift, luminosity distance, optical classification, SFR, AGN luminosity, AGN contribution to the bolometric luminosity ($\alpha_{\rm bol} = L_{\rm AGN}/L_{\rm bol}$), molecular and atomic gas content and radio parameter $q_{\rm IR}$ are listed in Table 1. This sample is homogenized as described in Sections 2.3 and 2.4, i.e. the properties of the host galaxy and the outflow are calculated in a consistent way across the entire sample. We stress that even though we have not used any other selection criteria, our sample is still heavily

Table 1. List of galaxies in the sample analysed in this paper, together with some of their basic properties.

Galaxy	Type	z	D_L (Mpc)	SFR ($M_\odot$ yr^{-1})	$\log(L_{AGN})$ (erg s^{-1})	$\log(M_\star)$ ($M_\odot$)	α_{bol}	$\log(M(H_2))$ ($M_\odot$)	$\log(M(HI))$ ($M_\odot$)	q_{IR}	Ref.
(1)	(2)	(3)	(4)	(5)	(6)	(7)	(8)	(9)	(10)	(11)	(12)
CO literature data											
IRAS F08572 + 3915	Sy2	0.05821	265	20	45.72	10.79	0.86	9.18		3.57	α, A, a
IRAS F10565 + 2448	Sy2	0.04311	196	95	44.81	10.66	0.170	9.90		2.64	α, A, a
IRAS 23365 + 3604	LINER	0.06438	285	137	44.67	11.23	0.072	9.93		2.73	α, A, a
Mrk 273	Sy2	0.03777	169	139	44.16	11.10	0.080	9.70	10.21	2.49	α, A, a
IRAS F23060 + 0505	Sy2	0.17300	831	75	46.06	11.75	0.780	10.39		2.79	α, A, a
Mrk 876	Sy1	0.12900	607	6.5	45.84	11.64	0.930	9.84		2.63	α, A, a
I Zw 1	Sy1	0.06114	259	36	45.37	11.30	0.520	9.56	10.27	3.04	α, A, a
Mrk 231	Sy1	0.04217	189	234	45.72	11.53	0.340	9.73		2.44	α, A, a
NGC 1266	LINER	0.00719	28.6	1.6	43.31	10.30	0.250	9.23		2.36	α, A, a
M82	H II	0.00068	4.03	10	$\leq$41.54	10.66	$\leq$0.0009	8.64	9.04	2.62	α, A, a
NGC 1377	LINER	0.00578	23.9	0.9	42.93	10.06	0.200	8.44	9.89		α, A, a
NGC 6240	Sy2	0.02448	107	16	45.38	11.53	0.780	9.86	10.05	2.10	α, A, a
NGC 3256	H II	0.00926	44.6	36	$\leq$41.97	11.23	$\leq$0.0007	9.68	9.89	2.37	α, A, a
NGC 3628	H II	0.00280	17.1	1.8	$\leq$40.79	11.30	$\leq$0.0009	9.53	10.31	2.00	α, A, a
NGC 253	H II	0.00081	2.77	3	$\leq$40.66	10.65	$\leq$0.0004	8.15	9.27	3.01	α, A, a
NGC 6764	LINER	0.00807	32.6	2.6	42.23	10.48	0.017	8.90	9.64	2.25	α, A, a
NGC 1068	Sy2	0.00379	13.1	18	43.94	11.23	0.097	9.11	9.12	2.32	α, A, a
IC 5063	Sy2	0.01100	47.2	0.6	44.30	11.02	0.9	8.85	10.75	1.11	α, A, a
NGC 2146	H II	0.00298	12.5	12	$\leq$41.09	10.58	$\leq$0.0003	8.94	9.41	2.83	α, A, a
IRAS 17208-0014	H II	0.0428	189	200	$\leq$43.67	11.33	$\leq$0.24	10.03		2.79	β, B, b
NGC 1614	H II	0.0159	68.3	45	$\leq$42.07	11.07	$\leq$0.0006	9.51		2.77	β, γ, C, b
Circinus Galaxy	Sy2	0.0014	8.34	0.6	43.57	10.95	0.59	9.32	10.27	2.07	δ, D, b
SDSS J1356 + 1026	Sy2	0.1230	579	20	46	11.36	0.43	8.91		2.32	ε, E, b
ESO 320-G030	H II	0.0108	51.1	20	$\leq$41.09	11.03	$\leq$0.0001	9.08		2.77	ζ, F, b
NGC 1808	H II	0.0033	10.8	5.1	$\leq$40.98	10.64	$\leq$0.0005	9.28	7.70		β, C, b
NGC 1433	Sy2	0.0036	14.5	0.23	42.24	10.67	0.20	8.63	9.22		η, G, b
M51	Sy2	0.0020	11.1	2.6	43.79	11.06	0.61	10.12	9.80	2.11	θ, H, b
4C 12.50	Sy2	0.1217	573	84	45.70	11.66	0.60	10.02		0.002	β,I,b,c
IRAS 05081 + 7936	H II	0.0537	239	98	$\leq$42.37	11.51	$\leq$0.0006	10.03		2.54	ι, J, d
IRAS 10035 + 4852	H II	0.0648	294	100	$\leq$45.11	11.19	$\leq$0.33	9.79		2.54	ι, J, d
IRAS F11119 + 3257	Sy1	0.189	929	144	46.2	12.20	0.689	9.94		1.62	κ, K, c
CO ALMA archival data											
IRAS 20100-4156	H II	0.129583	605	330	$\leq$42.93	11.10	$\leq$ 0.0007	9.95		2.93	σ, O, b
PG 0157 + 001	Sy1	0.16311	777	209	45.29	11.71	0.18	9.38		2.13	τ, P, b
IRAS 15115 + 0208	H II	0.095482	441	50.9	$\leq$43.49	11.96	$\leq$0.1	9.72			υ, J, b
IRAS 05189-2524	Sy2	0.042563	189	146	44.47	11.06	0.05	8.99		3.08	χ, Q, b
NGC 4418	Sy2	0.007268	36.4	14.5	43.81	10.22	$\leq$0.0005	8.59	8.66	3.35	η, S, b
IRAS 13120-5453	Sy2	0.030761	138	157	44.35	11.14	0.173	9.59			η, N, c, f
IRAS 22491-1808	H II	0.077760	348	145	$\leq$41.64	11.07	$\leq$0.06	10.22		3.26	ψ, Q, h
NGC 1386	Sy2	0.002895	11.1	0.27	40.19	10.03	0.0015	8.28		2.69	λ, L, b
NGC 6810	H II	0.006775	28	5.0	40.70	10.93	0.0003	8.86			μ, C, b
NGC 5643	Sy2	0.003999	20.1	3.6	42.91	10.90	0.0029	8.99	9.42		ν, H, b
OH outflows (González-Alfonso et al. 2017)											
IRAS F03158 + 4227	Sy2	0.13459	632	220	45.94	11.70	0.55				ξ, o, C, e
IRAS F14348-1447	LINER	0.08257	382	169	44.59	11.46	0.17	10.17			o, M, e
IRAS F14378-3651	LINER	0.067637	308	112	45.12	11.15	0.21	9.46		2.56	o, π, N, e
IRAS F20551-4250	LINER	0.04295	187	43	44.75	11.15	0.13	9.67		2.89	β, C, e

Notes. **Columns:** (1) Galaxy name, (2) optical classification, (3) redshift, (4) luminosity distance, (5) star formation rate, (6): AGN luminosity, (7) stellar mass, (8) fraction of the bolometric luminosity associated with the AGN ($\alpha_{bol} = L_{AGN}/L_{bol}$), (9) molecular gas mass, (10) H I gas mass, (11) radio excess parameter q_{IR}, galaxies with $q \leq 1.8$ have a radio excess, (12) references.
References: optical classification: α: Cicone et al. (2014), β: Yuan, Kewley & Sanders (2010), γ: Alonso-Herrero et al. (2001), δ: Neff et al. (1990), ε: Sun et al. (2014) and references therein, ζ: Pereira-Santaella et al. (2011), η: Véron-Cetty & Véron (2010), θ: Ho, Filippenko & Sargent (1997), ι: Leroy et al. (2015) and references therein, κ: Veilleux et al. (2002), λ: Lena et al. (2015), μ: Strickland (2007), ν: Cresci et al. (2015) and references therein, ξ: Nardini et al. (2010), o: González-Alfonso et al. (2017) and references therein, π: Teng et al. (2015), σ: Duc, Mirabel & Maza (1997), τ: Armus et al. (2004), υ: Best et al. (2005), ϕ: Baan, Salzer & LeWinter (1998), χ: Veilleux et al. (1995), ψ: Nardini et al. (2008) AGN luminosity/X-ray luminosity: A: Cicone et al. (2014) and references therein, B: García-Burillo et al. (2015), C: Brightman & Nandra (2011), D: Prieto et al. (2010), E: Sun et al. (2014), inferred from [O III] line, F: Pereira-Santaella et al. (2011), G:,Risaliti, Maiolino & Salvati (1999), inferred from [O III] line, H: Lutz et al. (2004), I: Teng et al. (2009), J: estimated upper limit from 6 μm flux according to Lutz et al. (2004), K: Tombesi et al. (2015), L: LaMassa et al. (2011), M: González-Martín et al. (2009), N: Teng et al. (2015), O: Franceschini et al. (2003), P: Piconcelli et al. (2005), Q: Severgnini, Maiolino & Salvati (2000) AGN contribution: a: Cicone et al. (2014) and references therein, b: calculated in this work, see Section 2.4, c: Veilleux et al. (2009), d: Leroy et al. (2015), e: González-Alfonso et al. (2017), f: Teng et al. (2015), g: Nardini et al. (2010), h: Nardini et al. (2008)

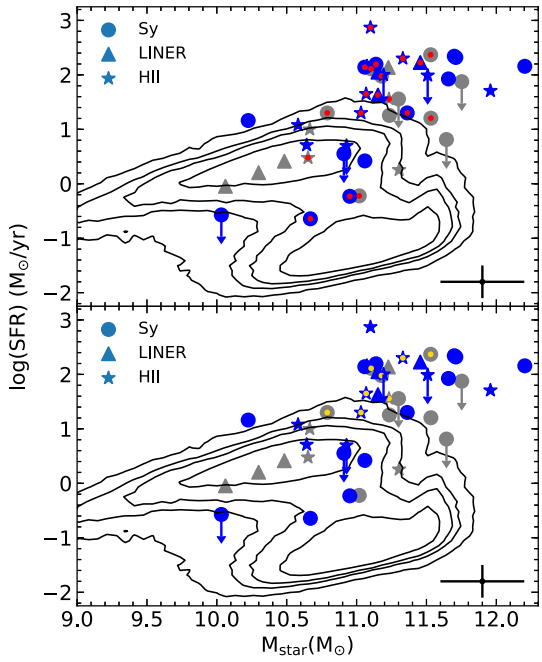

Figure 1. Distribution of our sample in the stellar mass–SFR diagram, compared to the SDSS galaxies (contours). The grey points show the galaxies in the sample of Cicone et al. (2014), the blue galaxies represent the additional galaxies added to that sample. The SDSS contours show the levels 100, 300, 500, 1000 galaxies. The red dot in the upper panel marks galaxies with measurements of ionized outflows, the yellow dot in the lower panel galaxies with observed neutral outflows.

biased, as most of the ALMA observing programmes (as well as results from the literature) have primarily targeted samples with enhanced star formation (ULIRGs or, more generally, starbursts) or with a known AGN. Nevertheless, we have significantly enlarged the sample relative to previous CO outflow studies by more than doubling its size and by including galaxies that are more representative of the massive star-forming galaxy population, as they feature also lower velocity outflows and much less extreme objects than in previous studies. In particular, we have included targets from the ALMA archive culled from observing programmes that were not aimed at extreme classes of galaxies (starbursts or AGN), and this has resulted in a less biased sample than in previous studies.

However, we emphasize, once more, that the goal of this paper is not to provide an unbiased census of the occurrence of molecular outflows in galaxies. The primary goal of this paper is to explore the relations between molecular outflows and galactic properties by sampling the broadest possible range of galactic properties, such as SFR, mass, activity type, AGN luminosity.

To illustrate the range of SFRs and galaxy stellar masses, Fig. 1 shows the galaxies in our sample in the stellar mass–SFR plane. We also overplot the contours of the distribution of galaxies from the Sloan Digital Sky Survey Data Release 7 (SDSS DR7) release, which shows the obvious biases affecting our sample. The grey points indicate galaxies from a previous study on molecular outflows by Cicone et al. (2014), the blue points show the new, additional galaxies added in this work. Different symbols indicate different optical spectral classification, as discussed more in detail later on. The sample spans about two orders of magnitude in stellar mass and nearly four orders of magnitude in SFR. Clearly, the galaxies in our sample are not distributed uniformly over these ranges and do not even follow the distribution traced by SDSS galaxies. As a consequence of the selection biases, our sample is skewed towards massive galaxies and mainly sampling galaxies above the main sequence, hence (probably merger-driven) 'starbursts'. However, our sample also probes the main sequence and a few galaxies located in the green valley. Unfortunately, quiescent galaxies are not included by our sample.

In addition, the fraction of AGN in our sample ($\approx$ 50 per cent) is higher than in other local complete surveys, where about 10–20 per cent are unambiguously AGN (although the actual number might be anything up to 40 per cent, depending on the AGN luminosity threshold and the selection band) (Maiolino & Rieke 1995; Miller et al. 2003). However, this enables us to properly probe different level and types of AGN activity. The AGN in our sample probe a wide range of bolometric AGN luminosities, from very weak AGN (10^{40} erg s^{-1}), to powerful AGN in the quasar regime (10^{46} erg s^{-1}).

2.2 Identification of outflows

The ALMA archival data have been calibrated and imaged using the CASA software version 4.7 (McMullin et al. 2007). We have ensured that the data cubes have a spectral window broad enough to find possible wings (covering at least 1500 km s^{-1}). We analyse the ALMA CO data initially by searching for outflow signatures by fitting a single or a double Gaussian profile to the CO emission integrated over the whole galaxy. Whether only one or two Gaussians are required is determined by comparing the reduced chi-square ($\chi^2_{\rm red}$) value of their respective fits. If two Gaussians lead to a decrease in $\chi^2_{\rm red}$ of 10 per cent or more, then we consider this as an initial clue for the possible presence of an outflow. In these cases, we also visually verify whether we can clearly distinguish a narrow ($\sigma_{\rm narrow} \lesssim 100$ km s^{-1}) and a broad component ($\sigma_{\rm broad}$ ranging from $\sim$100 km s^{-1} to several 100 km s^{-1}, depending on the galaxy). In these candidate cases, we tentatively identify the broad component as emission from an outflow as a first clue.

We then verify the presence of outflows by inspecting the position–velocity (pv) diagram and producing a map of the line wings. Position–velocity diagrams are generated by extracting a 2D spectrum along a pseudo-slit (with a typical width of about 0.6 arcsec) placed along the major and minor axes of the galaxy and plotting the velocity as a function of the position along the pseudo-slit. Rotation-dominated galaxies show a characteristic S-shape in the pv diagram (along the major axis), whereas outflows are identified by an excess of high-velocity gas on top of rotation. Line wings maps are also produced by integrating over the spectral range, where the broad component (i.e. outflow component) is dominant. We determine the root mean square (rms) of the line maps and identify the wings as significant when they are detected at a significance level of $>5\sigma$. The line wings are identified as due to outflows if they have velocities in excess of two times the width of the narrow component and are not located in the direction of rotation. In Appendix A, we show for each galaxy the spectrum integrated over the whole galaxy including the narrow and the broad component, the pv diagrams along the major and minor axes and the line maps of the wings.

2.3 Outflow properties

We calculate the outflow mass based on the flux of the broad-line component, which can be converted into $L'_{\rm CO}$, defined as

(Solomon & Vanden Bout 2005)

$$L'_{\rm CO} = 3.25 \times 10^7 S_{\rm CO}\Delta v \nu_{\rm obs}^{-2} D_{\rm L}^2 (1+z)^{-3}, \quad (1)$$

where $S_{\rm CO}\Delta v$ is the integrated flux in Jy km s^{-1}, $\nu_{\rm obs}$ is the observed frequency of the CO transition (in GHz), D_L is the luminosity distance (in Mpc), and z is the redshift. $L'_{\rm CO(1-0)}$ can in turn be converted into molecular mass of the outflow [$M_{\rm outf}(H_2)$] via $M_{\rm outf}(H_2) = \alpha_{\rm CO} L'_{\rm CO}$, where $\alpha_{\rm CO}$ is the CO-to-H_2 conversion factor. For outflows, we conservatively assume a CO-to-H_2 conversion factor of 0.8 $M_\odot/(K\,km\,s^{-1}\,pc^2)$ to for consistency with the previous work. This is the value typically adopted for the molecular ISM of ULIRGs (Bolatto, Wolfire & Leroy 2013). The excitation in the wings and the core in Mrk 231, a ULIRG hosting the closest QSO and a well-studied outflow were found to be very similar and hence the conversion factor in the non-outflowing and outflowing components are likely to be similar (Cicone et al. 2012). In some outflows, the conversion factor has been studied in detail (see e.g. Weiß, Walter & Scoville 2005; Cicone et al. 2018b), yielding values closer to $\alpha_{\rm CO} \approx 2\,M_\odot/(K\,km\,s^{-1}\,pc^2)$.

For outflows observed in higher-J transitions, we assume that the CO emission is thermalized and optically thick, hence $L'_{\rm CO(3-2)} = L'_{\rm CO(2-1)} = L'_{\rm CO(1-0)}$. This is consistent, within the errors, with what was found in Mrk 231 (Feruglio et al. 2015). The double-component fitting allows us to directly estimate the outflow velocity ($v_{\rm outf}$) using the prescription of Rupke et al. (2005a): $v_{\rm outf} = {\rm FWHM_{broad}}/2 + |v_{\rm broad} - v_{\rm narrow}|$, where FWHM$_{\rm broad}$ is the full width at half maximum of the broad component, and $v_{\rm broad}$ and $v_{\rm narrow}$ are the velocity centroids of the broad and narrow components, respectively. The spatial extent of the outflow is calculated based on the line maps of the broad wings. We fit a 2D-Gaussian profile to the wing map and use the beam-deconvolved major axis (FWHM) divided by two as the radius of the outflow.

The mass outflow rate, $\dot{M}_{\rm outf}(H_2)$, is calculated assuming time-averaged thin expelled shells or clumps (Rupke, Veilleux & Sanders 2005b):

$$\dot{M}_{\rm outf}(H_2) = \frac{v_{\rm outf}(H_2) M_{\rm outf}(H_2)}{r_{\rm outf}(H_2)}, \quad (2)$$

where $v_{\rm outf}(H_2)$, $r_{\rm outf}(H_2)$, and $M_{\rm outf}(H_2)$ are the velocity, radius, and molecular gas mass of the outflow, respectively. This description allows us a better comparison with models and is more realistic than the assumption of spherical (or multi-conical) volume with uniform filling factor (Cicone et al. 2015; Pereira-Santaella et al. 2016; Veilleux et al. 2017). It can be shown that between the two scenarios, there is a difference of a factor of 3 in the estimates of the outflow rate (and derived quantities such as kinetic power and momentum rate), which does not alter our conclusions significantly. Projection effects certainly plague the estimation of the outflow radius and velocity. However, as discussed in Cicone et al. (2015), since the orientations of outflows are distributed randomly, it can be shown that the resulting average correction factor is unity, hence statistically the (unknown) projection correction factors cancel out on average, though they certainly introduce scatter. By combining all sources of uncertainty, we infer that the average uncertainty on the mass outflow rate is about 0.3 dex. The errors on the associated outflow properties (kinetic power, momentum rate) is estimated to be as large as 0.5 dex. The outflow properties of all 45 galaxies are shown in Table 2. We provide mass outflow rate, outflow radius, outflow velocity and associated outflow properties. Furthermore, ionized and neutral mass outflow rate as well as escape fractions are also included in this table.

2.4 Ancillary information

In this section, we provide ancillary information on the host galaxy, which are summarized in Table 1.

2.4.1 Optical classification

In terms of activity classifications, we refer to galaxies as 'star forming', 'Seyfert', and 'LINER' based on their optical spectroscopic classification, and in particular through the BPT-[SII] diagram (Kewley et al. 2006). The nature of galaxies classified as 'LINER' is not always clear, and this classification appears to include a mixed population. It has been shown that the 'LINER' emission can extend on kpc-scales across a large fraction of passive and green valley galaxies (hence renaming this class as 'LIER', i.e. dropping the 'N' which stands for 'Nuclear' in the original acronym) and correlates with the old stellar population, and this can be explained in terms of excitation by the hard radiation field produced by evolved post-AGB stars (e.g. Sarzi et al. 2010; Belfiore et al. 2016). However, in the nuclear regions, LI(N)ER-like emission can also be associated with excitation by weak, radiatively inefficient AGN (e.g. Ho, Filippenko & Sargent 1993). Yet, in LIRGs, ULIRGs, and other galaxies characterized by prominent outflows, which are most of the LINER-like galaxies in our sample, LI(N)ER-like diagnostics are likely associated with shock excitation (e.g. Monreal-Ibero, Arribas & Colina 2006). Many authors broadly group Seyfert and LI(N)ER-like diagnostics into a generic 'AGN' category. As discussed above, this rough classification can be misleading as in many galaxies the LINER classification is not associated with an AGN at all; however, in the case of our sample, it is true that many LINER-like galaxies do host an AGN based on the X-ray or mid-IR properties; therefore in a few instances in the paper (e.g. Section 3.2), we will adopt this classification as well. Regardless of the optical classification, the role of the AGN, if present, will be clarified by the AGN fractional contribution to the bolometric luminosity, as discussed in the following.

2.4.2 AGN luminosity

AGN bolometric luminosities were derived from the hard X-ray flux (2–10 keV) by using the relation given in Marconi et al. (2004): $\log[L_{\rm AGN}/L\,(2\text{–}10\,{\rm keV})] = 1.54 + 0.25\mathcal{L} + 0.012\mathcal{L}^2 - 0.0015\mathcal{L}^3$, where $\mathcal{L} = (\log L_{\rm AGN} - 12)$ and $L_{\rm AGN}$ is the AGN bolometric luminosity in units of $L_\odot$. Typically, X-ray-based AGN luminosities have a scatter of ~ 0.1 dex (Marconi et al. 2004). In a few cases where no X-ray data are available, or the source is Compton-thick, we used the [O III]λ5007 luminosity. In this case, the AGN luminosity is inferred from the relation $L_{\rm AGN} \sim 3500\,L_{\rm [O\,III]}$ (Heckman et al. 2004). In some cases for which [O III]λ5007 is not available, or which are heavily obscured in the optical, we estimated the AGN luminosity by using the AGN contribution to the bolometric luminosity $\alpha_{\rm bol}$ as inferred from various mid-IR diagnostics in the literature (Nardini et al. 2009, 2010; Veilleux et al. 2009). Nardini et al. (2009, 2010) use spectral features in the wavelength range of 5–8 μm that allow them to disentangle AGN and starburst contribution. Veilleux et al. (2009) use six different IR-based methods, as for instance the equivalent width of the PAH feature at 7.7 μm and the continuum ratio of f_{30}/f_{15}, and average them to calculate the AGN contribution. Using the AGN fraction, we can then calculate the AGN luminosity via $L_{\rm AGN} = \alpha_{\rm bol} L_{\rm bol}$, where in most cases $L_{\rm bol} \approx L_{\rm IR}$ (although for ULIRGs $L_{\rm bol} \sim 1.15\,L_{\rm IR}$ (Veilleux et al. 2009)). In the rest of the paper, $\alpha_{\rm bol} = L_{\rm AGN}/L_{\rm bol}$ refers to the AGN

contribution to the total IR luminosity, which generally dominates in most of our galaxies, although in a few more quiescent galaxies the stellar optical/NIR light may contribute significantly. The uncertainty of the IR luminosity consists of the contribution from uncertainties on the IR fluxes at 12, 25, 60, and 100 μm, which are generally below 10 per cent and the scatter in the calculation of the total IR luminosity, $L_{\rm IR}$, based on these IRAS fluxes, which is about 10–20 per cent (Takeuchi et al. 2005). In total, we therefore conservatively assume 30 per cent uncertainty on $L_{\rm IR}$.

2.4.3 Star formation rate

To compute the total star formation, we use the $L_{\rm IR}$–SFR relation given in Kennicutt & Evans (2012), which assumes a Chabrier initial mass function (IMF) and the total IR luminosity from 8 to 1000 μm, corrected for the AGN contribution through the $\alpha_{\rm bol}$ factor. The uncertainty in SFRs stems from uncertainties on $L_{\rm IR}$ (which is discussed above and amounts to ∼30 per cent) and on $\alpha_{\rm bol}$. $\alpha_{\rm bol}$ has similarly values using various techniques and they usually agree within 10–15 per cent (Veilleux et al. 2009). We assume this as the typical error. The conversion of IR luminosity to SFR comes with a 30 per cent calibration uncertainty (Kennicutt 1998). For SFR estimates, we therefore infer conservatively a typical uncertainty of 0.3 dex.

2.4.4 Gas content

The molecular gas mass in the host galaxy is inferred from the CO(1–0) (narrow) line luminosity $L'_{\rm CO}$, as discussed above. The CO-to-H_2 conversion factor is one of the major uncertainties in the calculation of the molecular gas mass and depends heavily on the metallicity and physical state of the molecular ISM (Bolatto et al. 2013). We adopt three different CO-to-H_2 conversion factors depending on the type of galaxy. For ULIRGs, we adopt $\alpha_{\rm CO} = 0.8\ {\rm M}_\odot/({\rm K\,km\,s^{-1}\,pc^2})$, for LIRGs we use $\alpha_{\rm CO} = 1.2\ {\rm M}_\odot/({\rm K\,km\,s^{-1}\,pc^2})$, and for all other galaxies, we use a Milky Way-type conversion factor of $4.4\ {\rm M}_\odot/({\rm K\,km\,s^{-1}\,pc^2})$ (Bolatto et al. 2013).

For about half of the galaxies 21 cm H I, single dish, observations are also available that provide the atomic gas mass in the host galaxy.

2.4.5 Stellar mass

Stellar masses are calculated for all galaxies in this sample by using the *K*-band magnitude and a colour correction (e.g. $B-V$) (Bell et al. 2003). *K*-band magnitudes are taken from the extended source catalogue of 2MASS (Skrutskie et al. 2006).

However, the presence of an AGN can potentially contaminate the observed fluxes. For Seyfert 2 galaxies, the direct continuum radiation from the accretion disc is obscured along our line of sight, but the hot dust heated by the AGN can still contribute significantly to the light observed in the *K* band. Therefore, in the case of Seyfert 2 galaxies, in order to avoid the latter issue, we use *J*-band magnitudes that are not affected by AGN-heated circumnuclear dust emission, and estimate the *K*-band magnitude by assuming $J–K = 0.75$, which is the average colour (with little scatter) found by Mannucci et al. (2002).

For Seyfert 1 galaxies in our sample, a contamination by the AGN might be very high also in the *J* band and optical bands (because the radiation from the accretion disc is directly observable) and, therefore, we need to use a different approach. For Mrk 231 and IRAS F11119 + 3257, the contribution of the AGN to the total magnitudes has been estimated in Veilleux, Kim & Sanders (2002) and we simply subtract this nuclear contribution to estimate the stellar masses in these two galaxies. For the other three Seyfert 1 galaxies, we compute the stellar mass by using the *H*-band magnitude of the host (which does not include nuclear contribution by the AGN) inferred by Zhang et al. (2016) and the mass-to-light correction given in their paper.

For non-type 1 AGN, the colours for the mass-to-light ratio correction are obtained from the literature. We combine different colours, $u-g$ for galaxies with SDSS photometry, $B-V$ from VERONCAT, the Veron Catalogue of Quasars and AGN (Véron-Cetty & Véron 2010), or from the GALEX survey (Gil de Paz et al. 2007) and $B-R$ from the APM catalogue.[1] In a few cases where no information about colours is available, we assume an average logarithmic mass-to-light correction of −0.08 (Bell et al. 2003; Zhang et al. 2016). Our final errors on the stellar mass comprises errors on the photometry of the host galaxy (*H*, *J*, or *K* band) and the uncertainty of the $M_\star/L$ ratio. The *K*-band magnitudes are estimated to have an 0.1 mag uncertainty based on comparison between different samples (Bell et al. 2003). In the *J* and *H* bands, the typical uncertainty is 0.2 mag (Zhang et al. 2016). Our estimates of $M_\star/L$ ratios have a typical systematic error of about 25 per cent that stems from uncertainties in galaxy age, dust extinction, and the impact of SF bursts on the star formation history (Bell et al. 2003). Furthermore, for AGN host galaxies, additional uncertainties might be introduced by the corrections applied here. Therefore, we conservatively obtain an average error of ±0.2 dex on the stellar masses. Although the use of different colours for some of the galaxies may potentially be a matter of concern, Bell & de Jong (2001) and Taylor et al. (2011) have shown that there is no systematic uncertainties on the inferred stellar masses when different colours and different (IR/red) bands are used.

2.4.6 Radio emission

In order to investigate the potential link between outflows and radio jets, we have also collected data about the radio power in galaxies at 1.4 GHz, mostly by using the data base provided by NED. Since in normal star-forming galaxies the radio luminosity simply scales with the SFR as traced by the IR luminosity (e.g. Yun, Reddy & Condon 2001; Ivison et al. 2010), the contribution from a radio jet can be inferred in terms of excess relative to the radio-to-IR ratio observed in normal star-forming galaxies. Therefore, in Table 1, we provide the quantity $q_{\rm IR}$ that is the ratio between the rest frame 8–1000 μm flux and the 1.4 GHz monochromatic radio flux (Ivison et al. 2010).

2.5 Ionized outflows

We complement our results on molecular outflows with data on the ionized outflow phase. For each galaxy, we search whether a reliable estimate of the ionized outflow mass is provided in the literature. 16 of our sources, i.e. about one-third of the sample, have measurements of the ionized outflow mass, velocity, and radius. Rupke & Veilleux (2013) provide ionized gas masses for four galaxies (IRAS F08572+3915, IRAS F10565 + 2448, Mrk 273, and Mrk 231) based on the H α emission. Greene, Zakamska & Smith (2012) estimate the ionized outflow mass for SDSS J1356 + 1026 using H β.

[1] http://www.ast.cam.ac.uk/∼mike/apmcat/

The other sources with ionized outflow rates are taken from Arribas et al. (2014) and are based on integral field spectroscopy (IFS) of H α.

We carefully homogenize the calculations of the ionized outflow properties. Outflow velocities are calculated in the same way as for the molecular outflow, i.e. $v_{\rm outf}({\rm ion}) = {\rm FWHM}_{\rm broad}({\rm ion})/2 + |v_{\rm broad}({\rm ion})\text{-}v_{\rm narrow}({\rm ion})|$ (Rupke et al. 2005a). For the calculation of the outflow mass, $M_{\rm outf}$(ion), we assume an electron density of $n_{\rm e} = 315$ cm^{-3} as found in Arribas et al. (2014). This value is also close to the electron density values found in other works (e.g. Perna et al. 2015; Bischetti et al. 2017). We calculate the ionized outflow mass rate as follows:

$$\dot{M}_{\rm outf}({\rm ion}) = \frac{v_{\rm outf}({\rm ion}) M_{\rm outf}({\rm ion})}{R_{\rm outf}({\rm ion})}, \quad (3)$$

where $R_{\rm outf}$(ion) is the radius of the outflow. For the outflow extent, we generally assume the same value given in the corresponding paper. However, in Arribas et al. (2014), an average fixed radius of 700 pc is assumed. Instead of using this fixed radius, we use the value inferred from Bellocchi et al. (2013) using the broad H α maps obtained with VIMOS at the Very Large Telescope (VLT) and assuming a spherical geometry.

We note that the spatial extent of ionized outflow can be severely affected by beam smearing effects, because the observed spatial distribution is luminosity weighted, hence the central, compact regions dominate the outflow size measurement, even if the outflow is much more extended. This results in an overestimation of the outflow rate. Indeed, the uncertainty on the outflow extent (limited by the typical seeing of about 1 arcsec), often resulting into an error of 50 per cent on the outflow radius, dominates the uncertainty on the outflow rate shown in the various figures.

Measurements of the ionized outflow are available for only one-third of the sample. Galaxies in our sample with ionized outflow measurement are indicated with a red dot in the top panel of Fig. 1. Unfortunately, the part of the sample with available ionized outflow information is restricted to the mass range of $10.4 < \log(M_*/M_\odot) < 11.6$, hence limiting our capability to properly explore the full mass range probed by the molecular outflow sample. However, within this mass range, the galaxies with ionized outflows sample the full SFR range.

2.6 Neutral outflows from Na ID

We also include data on neutral atomic outflows in the same way as for the ionized outflows. We cross-match our sample with Rupke & Veilleux (2013) and Cazzoli et al. (2016), where the properties of the neutral outflow are inferred from the blue-shifted neutral sodium absorption doublet lines (Na ID) at 5890 and 5896 Å. The Na ID absorption method can only trace outflows towards those lines of sights that have enough stellar continuum light in the background; this often limits the use of this diagnostic to the central regions of galaxy discs. Additional issues affecting this diagnostics is that it has to be disentangled from the Na ID stellar absorption, from possible Na ID emission and from the nearby He I nebular emission.

With these caveats in mind, we have taken the outflow rate inferred in the original papers. We have also attempted to re-determine the outflow rate by taking the outflow mass given in the original papers and re-calculating the outflow by using our approach, based on size and outflow velocity, although in this case the method is not fully applicable as the covering factor is another parameter that should be taken into account. In most cases, we obtain values close to those reported in the original papers, however, for a couple of galaxies the difference is as high as a factor of 3. We will use both the atomic outflow rate reported in the original papers and those recalculated by us.

2.7 Neutral outflows from [C II]

The fine-structure transition of C^+, [C II], is another tracer of cold neutral gas, which has been increasingly used to search outflows, especially at high redshift (Maiolino et al. 2012; Cicone et al. 2015; Janssen et al. 2016; Gallerani et al. 2018). The majority of [C II] emission is believed to stem from photon-dominated regions (PDRs), where the bulk of the gas is in the neutral atomic phase. However, about 20 per cent is generally coming from CO-dark molecular gas and about 30 per cent can come from the partly ionized phase (Pineda, Langer & Goldsmith 2014). We have collected data on the [C II]-outflow for our sample from Janssen et al. (2016), who provide the atomic mass in the outflow based on the [C II] broad/narrow components decomposition, assuming a temperature of 100 K and density of 10^5 cm^{-3}, which should be typical of the ULIRGs in their sample. The outflow rate is then calculated by taking the radius estimated from the CO observations and consistently with the method used for molecular outflows, as described above. As we will see in the next section a few targets have measurements of atomic neutral outflows both from Na ID and [C II]. In some of these cases, the agreement between the measured mass-loss rates is within a factor of 2, which is remarkable given all assumption, potential systematics and issues discussed above. However, for one ULIRG hosting a powerful AGN (Mrk 273), the difference is as large as an order of magnitude, hinting at the fact that for some extreme targets the uncertainties in the estimation of the atomic neutral outflow can be very large.

Combining the measurements of atomic neutral outflows from Na ID and [C II] measurements (also taking into account galaxies that have both measurements) only 12 galaxies have this information (about one-fourth of the full sample). These are indicated with a yellow dot in the bottom panel of Fig. 1. They span the limited mass range $10.6 < \log(M_*/M_\odot) < 11.6$, and only probe galaxies with high SFR (generally higher than the main sequence), implying that the atomic neutral outflows in our sample are hardly representative of the broader population of galaxies (in terms of mass and SFR), probed by the full sample with molecular outflow information. The extrapolation of the atomic neutral information to the full sample should be considered with great care, and possibly expanded in the future.

3 RESULTS

In this section, we report the main results obtained through our sample of molecular outflows, in combination with the ancillary data. A more extensive analysis of the results and of their interpretation is given in Section 4.

3.1 Atomic neutral and ionized outflows in comparison with molecular outflows

We start by investigating the relation between molecular outflow rate and atomic neutral and ionized outflow rates for those galaxies in our sample that have additional multiwavelength data suited for such a study.

In Fig. 2, we plot the molecular outflow rate as a function of ionized outflow mass rate of the same object, for those galaxies that have information on *both* outflow phases available. Star-forming

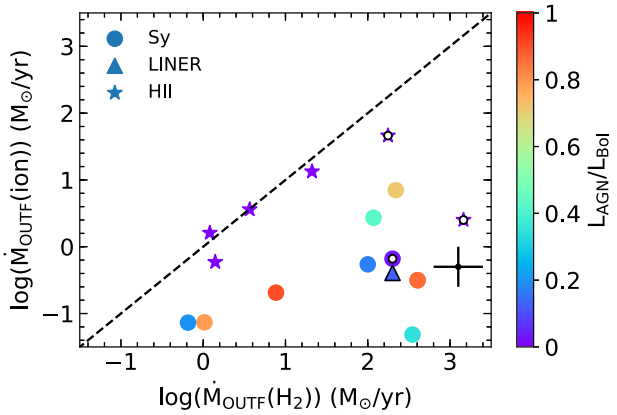

Figure 2. Molecular outflow mass rate [$\dot{M}_{\rm outf}(H_2)$] compared to the ionized outflow mass rate [$\dot{M}_{\rm outf}$(ion)]. The dashed line shows the 1:1 relation. Circles indicate Seyfert host galaxies, LINERs are plotted as triangles and purely star-forming galaxies as stars. The data points are colour-coded according to their AGN contribution ($L_{\rm AGN}/L_{\rm bol}$), as given in the colour bar on the right. The data points with black edges are molecular outflows inferred from OH measurements by González-Alfonso et al. (2017). The symbols with a central white dot are the candidate 'fossil' outflows (see Section 4.3).

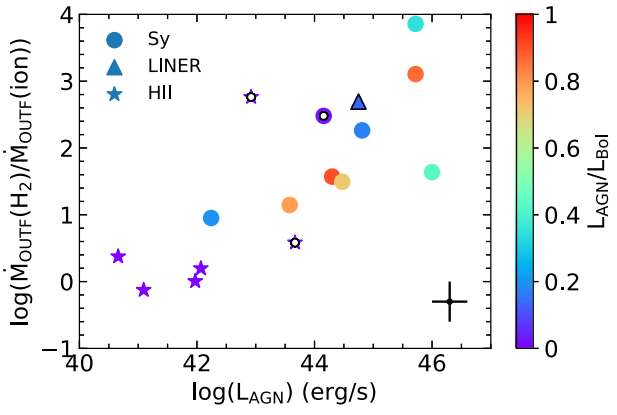

Figure 3. Molecular to ionized mass outflow rate as a function of AGN luminosity. Colour-coding and symbols are same as in Fig. 5.

galaxies have comparable ionized and molecular outflow rates. As we will see, the molecular outflow loading factor for star-forming galaxies is close to one, implying that also the ionized outflow loading factor is close to unity, in agreement with independent studies focused specifically on ionized outflows (Heckman et al. 2015).

In contrast, AGN host galaxies have much higher molecular outflow rates than ionized ones. This is in agreement with previous studies (Rupke & Veilleux 2013; García-Burillo et al. 2015; Carniani et al. 2015; Fiore et al. 2017), which observed that molecular outflow rates are 2–3 mag higher than ionized outflow rates. Rupke et al. (2017) also investigate the multiphase outflow in a few quasars; only two objects in their sample have measurements in the molecular phase, and in these two cases, the molecular phase dominate the outflow mass relative to the atomic phase.

At higher AGN luminosities (above 10^{46} erg s^{-1}), it has been suggested that the ionized winds have similar mass outflow rates to molecular winds (Fiore et al. 2017); however, these previous studies were mostly based on the comparison of galaxy samples that were observed in different gas phases. It is difficult to directly investigate the relation between molecular and ionized gas in luminous, distant quasars, as it generally very challenging to detect their molecular outflows through their weak CO wings, which are in most cases still below the detection limits, even for ALMA observations, for most high-z QSOs. The few deep ALMA/NOEMA observations and studies reported so far on some individual quasars are not conclusive yet. Brusa et al. (2018) have reported the detection of a molecular (CO) outflow rate comparable with the ionized outflow rate in a quasar at $z\sim1.5$, while Toba et al. (2017) have reported the lack of molecular (CO) outflow in an AGN at $z\sim0.5$. However, in both cases the sensitivity of the millimetre observation is still far from what would be required to match the optical/near-IR observations, hence a significant amount of outflowing molecular gas may still be missed in these observations. Carniani et al. (2017) have reported the detection of a molecular outflow in a quasar at $z\sim2.3$, having an outflow rate much larger than the ionized outflow rate. Feruglio et al. (2017) have reported the detection of a fast and massive molecular outflow [$\dot{M}_{\rm outf}(H_2) = 3$–$7\times10^3\,M_\odot{\rm yr}^{-1}$] in a lensed quasar at $z\sim4$, but unfortunately in this case the ionized outflow rate is not available for comparison. Although, it is not yet possible to make a direct, statistically sound comparison of the ionized and molecular outflow rates at very high luminosities, we can at least investigate the relationship and trend within the luminosity range probed by our sample. Fig. 3 shows the dependence of the ratio between molecular and ionized outflow rate as a function of the bolometric luminosity of the AGN. The ratio $\dot{M}_{\rm outf}(H_2)/\dot{M}_{\rm outf}$(ion) clearly increases with AGN luminosity, which is the opposite trend of that obtained in the past based on disjoint samples of ionized and molecular outflows (Fiore et al. 2017). However, our sample is still small and does not reach up to very high AGN luminosities ($>10^{46}$ erg s^{-1}). Yet, overall our data confirm the results of Fiore et al. (2017) and Carniani et al. (2015) that, in our luminosity range ($L_{\rm AGN}<10^{46}$ erg s^{-1}), molecular outflows have outflow rates about two order of magnitude larger than ionized outflow rates.

Neutral atomic gas can be measured through the Na ID absorption, but it is subject to significant uncertainties due to the fact that it can be probed only where there is enough background stellar light. Moreover, disentangling the Na ID absorption outflow feature from the Na ID stellar absorption and from the ISM absorption in the host galaxies, as well as from the He I an Na ID nebular emission, further increases the uncertainties. An alternative way to probe the atomic neutral outflow is to exploit the fine-structure line of C^+, [C II]λ157.74 μm, which, as discussed in Section 2.7, traces primarily atomic gas. Janssen et al. (2016) measured the outflowing mass of atomic gas in a sample of ULIRGs/LIRGs some of which are in our sample, and for which we have inferred the atomic outflow rate as discussed in Section 2.7. In Fig. 4, we compare the atomic outflow mass rate inferred from both [C II] and Na ID (surrounded by a black square) with the molecular outflow rate from this work for galaxies with measurements of both tracers. The sample size is small so far. Despite this, the inferred atomic outflow rates of AGN host galaxies seem to be very similar to the molecular outflow rates, suggesting that outflows have similar contribution of atomic neutral and molecular gas. For star-forming galaxies, the outflow masses are comparable in the atomic and molecular phase, but any possible trend is likely washed out by the above-mentioned uncertainties. The discrepancy between the Na ID and the carbon measurements can be explained in the uncertainties associated with Na ID discussed above, though more observations are needed to investigate these issues.

With the limited statistics available for the sub-samples with multiple outflow phases, it is not possible to provide accurate rela-

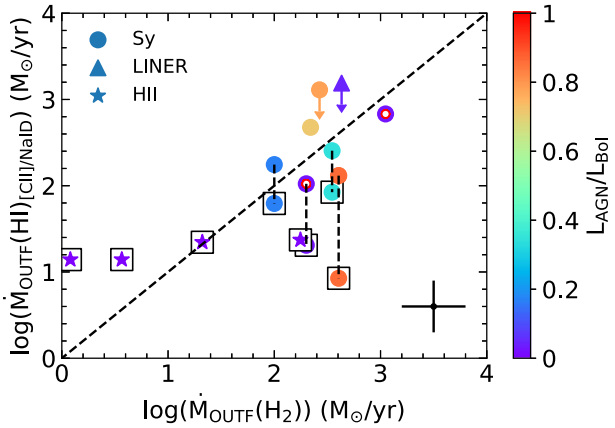

Figure 4. Neutral atomic outflow rates inferred from the [C II] line or the Na ID absorption (outlined using black squares) as a function of the molecular outflow rates. Measurements of the same galaxy obtained with two different methods ([C II] or Na ID) are connected with a dashed black line. The diagonal dashed line gives the 1:1 relation. Colour-coding and symbols are same as in Fig. 2.

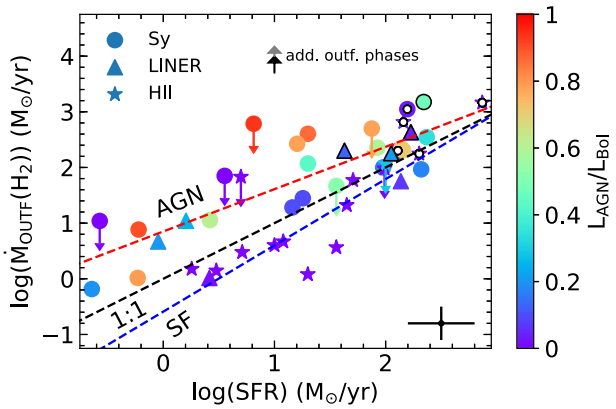

Figure 5. Mass outflow rate as a function of SFR. The black dashed line shows the relation for an outflow mass-loading factor $\eta = \dot{M}_{outf}(H_2)/SFR = 1$. The black dashed line is the 1:1 relation between outflow rate and SFR, i.e. $\eta = 1$. The red and blue dashed lines represent the best fits to AGN hosts and star-forming/starburst galaxies, respectively. The vertical black and grey arrows indicate the average correction of the outflow rate, for AGN and star-forming galaxies, respectively, once the atomic (ionized and neutral) phase average contributions to the outflow rate (as inferred in Section 3.1) are included. Colour-coding and symbols are same as in Fig. 2.

tionships among the various phases, also because there is significant dispersion. However, it is useful to provide some indication on the rough relationship between the molecular outflow and other two phases, which can provide some guidance on how to obtain the *total* outflow rate (and other derived quantities) to correct the molecular outflow rate by roughly accounting for the additional phases. Based on the above results, we can roughly state that in starburst-driven outflows the ionized and neutral atomic phases contribute, each of them, to the outflow rate at the same level as the molecular outflow rate. In AGN-driven outflows, the atomic neutral outflow rate is similar to the molecular outflow rate, while the ionized outflow rate is negligible. We will adopt these simple recipes, when attempting to infer the global properties of outflows in the following sections.

3.2 Mass outflow rate scaling relations

In this section, we start investigating the scaling relations between the molecular outflow rate and galaxy properties, with the goal of obtaining a first indication of the driving mechanism in different regimes.

3.2.1 Dependence on SFR and L_{AGN}

Fig. 5 shows the molecular mass outflow rate $\dot{M}_{outf}(H_2)$ as a function of the SFR, colour-coded by AGN contribution to the bolometric luminosity. Similar to what was found in smaller samples in previous works (Cicone et al. 2014; García-Burillo et al. 2015), the star-forming/starburst galaxies have a mass-loading factor $\eta = \dot{M}_{outf}(H_2)/SFR$ consistent with unity or slightly lower. As we have discussed in the previous section, in star-forming galaxies the contribution to the total mass-loss rate is similar for different gas phases (ionized/neutral atomic and molecular). By including all the gas phases, the total mass-loss rate increases roughly by 0.5 dex, which is indicated by the grey arrow, and which brings the total loading factor closer to (or exceeding) unity for star-forming galaxies. However, for the moment we focus on the molecular outflow rate. The best fit of the relation between molecular outflow rate and SFR for SF galaxies (shown as a dashed blue line in Fig. 5) is $\log(\dot{M}_{outf}(H_2)/(M_\odot\ yr^{-1})) = 1.19^{+0.16}_{-0.16}\log(SFR/(M_\odot\ yr^{-1})) - 0.59^{+0.28}_{-0.28}$. This and the following fits are performed by using linmix (Kelly 2007), considering the error bars both in x and y and including upper limits.

The AGN host galaxies have a mass-loading factor larger than unity, especially those that are AGN dominated, and η ranges from a factor of a few up to a hundred. The best-fitting relation for AGN host galaxies is $\log(\dot{M}_{outf}(H_2)/(M_\odot\ yr^{-1})) = 0.76^{+0.11}_{-0.11}\log(SFR/(M_\odot\ yr^{-1})) + 0.85^{+0.18}_{-0.18}$ and is shown with a red dashed line in Fig. 5. As we have discussed in the previous subsection, in AGN host galaxies the atomic phase makes, on average, a comparable contribution to the outflow rate as the molecular phase, while the ionized phase is generally negligible, at least in the luminosity range probed by us. The effect of including the atomic component of the outflow for AGN is shown with a black arrow.

The outflow properties inferred in star-forming galaxies are in good agreement with models predicting a mass-loading factor η close to 1 (e.g. Finlator & Davé 2008; Davé, Oppenheimer & Finlator 2011; Heckman et al. 2015), where feedback from supernovae (SNe) is the main outflow driver and required to properly regulate star formation in galaxies.

Galaxies containing an AGN have loading factors larger than 1, indicating that gas is removed at a faster rate than stars are formed. In particular, the presence of a strong AGN in the galaxy increases the (molecular) outflow mass loading-factor substantially. In particular, the higher the AGN contribution (α_{bol}, see colour-coding in Fig. 5), the higher their mass-loading factor η. This is illustrated even more clearly in Fig. 6, where the relation between the outflow loading factor, i.e. $\eta = \dot{M}_{outf}(H_2)/SFR$ and $\alpha_{bol} = L_{AGN}/L_{bol}$, is shown. However, a correlation is seen only at $L_{AGN}/L_{bol} > 0.7$, while at $0.1 < L_{AGN}/L_{bol} < 0.7$, the loading factor η simply scatters between 1 and 10 for AGN. As we will discuss further later on, this is probably due to two effects: (1) additional contribution from star formation to the outflow rate (which, however, is expected to contribute only with $\eta \sim 1$); (2) the fact that the outflow has much longer time-scale ($>10^6$ yr) than the AGN accretion variability ($\sim$10–10^5 yr) (Gilli et al. 2000; Schawinski et al. 2015), hence the

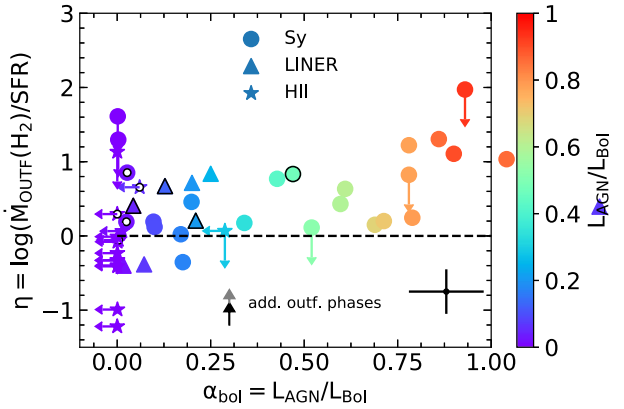

Figure 6. Mass loading factor $\eta = \dot{M}_{outf}(H_2)/SFR$ as a function of AGN fractional contribution to the bolometric luminosity, L_{AGN}/L_{bol}. The black dashed line shows the relation for an outflow mass-loading factor $\eta = 1$. Colour-coding and symbols are same as in Fig. 2.

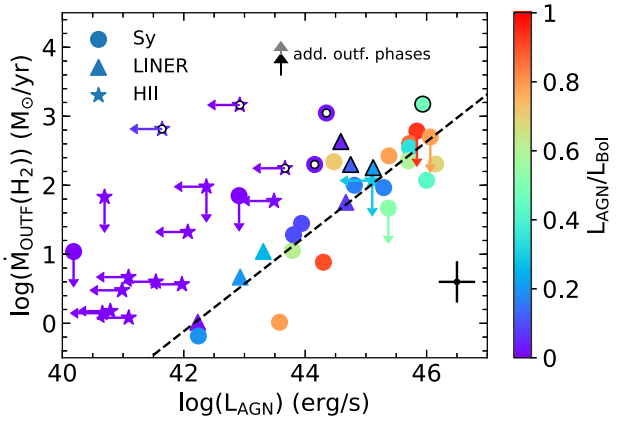

Figure 7. Mass outflow rate as a function of AGN (bolometric) luminosity. The dashed line indicates the fit to the AGN host galaxies (LINERs, Seyfert 1 and 2). Colour-coding and symbols are same as in Fig. 2.

outflow is expected to generally outlast an AGN that has recently switched off, or decreased in luminosity.

Fig. 7 shows the correlation between the mass outflow rate and L_{AGN}. The dashed line shows the best fit to the AGN host galaxies (LINERs, Seyfert 1 and Seyfert 2), excluding purely star-forming galaxies (optically classified as star forming/starburst), which gives the following relation: $\log(\dot{M}_{outf}/(M_\odot\ yr^{-1})) = 0.68^{+0.10}_{-0.10}\log(L_{AGN}/(erg\ s^{-1})) - 28.5^{+4.6}_{4.6}$. Comparing with the predictions from chemo-hydrodynamic simulations (Richings & Faucher-Giguère 2018), the observed values are about 1 dex higher at $L_{AGN} = 10^{44}$ erg s^{-1}, but are consistent with simulations at $L_{AGN} \approx 10^{46}$ erg s^{-1} within the errors. Although Seyfert galaxies show a correlation between AGN luminosity and molecular outflow mass rate, suggesting that these outflows are AGN driven, this correlation is looser and with larger scatter than previously found in the literature (e.g. Cicone et al. 2014; Fiore et al. 2017), probably as a consequence of our sample being less biased. Nevertheless, this is still supportive of the scenario in which luminous AGN boost the outflow rate by a large factor and nearly proportionally to the AGN radiative power. It is interesting to note that Fig. 7 clearly shows the presence of a significant fraction of galaxies (indicated by symbols with a central white dot) with high outflow rates but little AGN contribution and, for those classified as AGN, clearly not

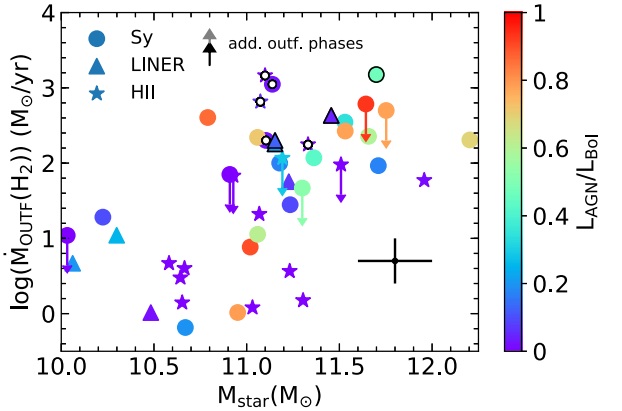

Figure 8. Molecular outflow mass rate as a function of galaxy stellar mass. Colour-coding and symbols are same as in Fig. 2.

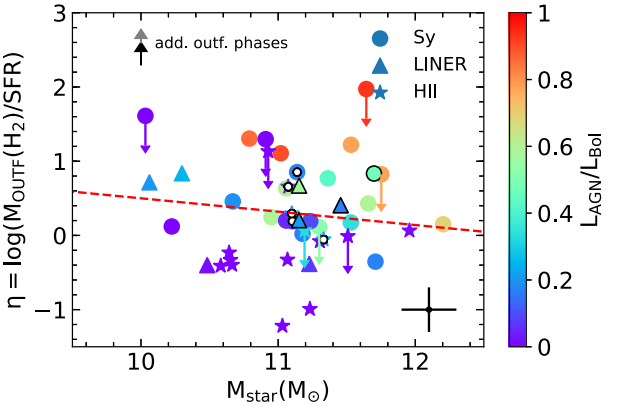

Figure 9. Mass-loading factor as a function of stellar mass. The red dashed line shows the best fit to the data. Colour-coding and symbols are same as in Fig. 2.

following the correlation observed for the bulk of luminous AGN host galaxies. As discussed above, this is partly due to contribution by star formation, but the bulk of the effect may be due to 'fossil' AGN-driven outflows as it will be clarified in the Section 4.

3.2.2 *Dependence on galaxy stellar mass*

Fig. 8 shows the outflow rate as a function of stellar mass. This plot shows some correlation, which may be indirectly linked to the correlation between outflow rate and SFR, through the stellar mass–SFR relation for galaxies on the 'main sequence'. An important prediction of theoretical models of feedback from star formation is that the outflow loading factor should anticorrelate with the galaxy stellar mass as $\eta \propto M_\star^{-0.5}$, as a consequence of the deeper gravitational potential well in more massive galaxies (Mitra, Davé & Finlator 2015; Somerville & Davé 2015; Chisholm et al. 2017). Fig. 9 shows the dependence of the mass loading factor η on the stellar mass. Clearly, the observed relation between outflow mass-loading factor and stellar mass is very scattered. A linear regression indicates that there is only a weak anticorrelation of the form $\log(\eta) = -0.18^{+0.24}_{-0.24}\log(M_\star/M_\odot) + 2.3^{+2.7}_{-2.6}$, i.e. only marginally consistent with theoretical predictions. However, before invoking any tension with theoretical models one should be aware of three main issues: (1) we include AGN-driven and star formation-driven outflows, whereas the models make predictions about outflows driven by SNe and

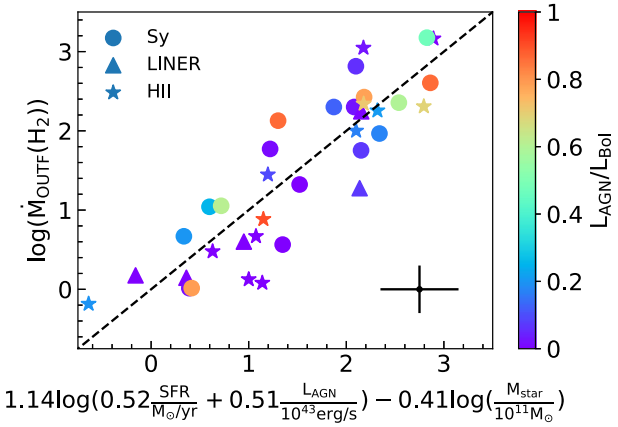

Figure 10. Simultaneous multiple linear regression fit of the molecular outflow rate as a function of SFR, stellar mass, and AGN luminosity, as given in equation (5). Colour-coding and symbols are same as in Fig. 2.

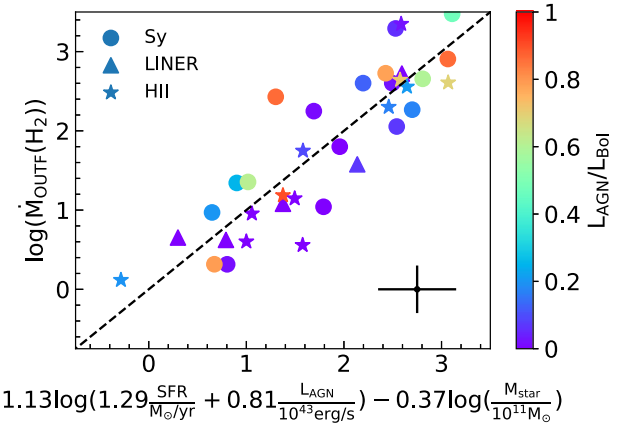

Figure 11. Simultaneous multiple linear regression fit of the *total* outflow rate as a function of SFR, stellar mass, and AGN luminosity, as given in equation (6). Colour-coding and symbols are same as in Fig. 2.

stellar radiation pressure, (2) the range of stellar masses is probably too narrow to properly test the theoretical predictions, especially given that the dependence of the outflow rate on mass is weak (slope of –0.5 in log); (3) thirdly, the simple relation of outflow rate with stellar mass is convolved with the dependence on SFR and with the AGN contribution, which likely dominate the scatter of any relation with $M_\star$. We address the last issue in the following subsection.

3.2.3 Disentangling the outflow dependence on host galaxy parameters

In the previous subsections, we have shown how the outflow rate depends on galaxy properties (for which sensitive CO observations are available, such as stellar mass, SFR, and the luminosity of the AGN). However, it is difficult to isolate the role played by each of these quantities, especially given that they are correlated. In this section, we attempt to disentangle the contribution of these different factors.

For this purpose, we performed a regression as follows:

$$\log(\dot{M}_{\rm outf}) = x\ \log(\alpha{\rm SFR}+\beta L_{\rm AGN}) + y\ \log M_\star, \quad (4)$$

and finding the values of the parameters that minimize the dispersion around this relation. The reason for using this expression is that for starburst galaxies we only have an upper limit on the AGN luminosity. Combining the SFR and AGN in the term in parenthesis ensures that this term never diverges to very negative values in log, i.e. it ensures that when we investigate galaxies with outflow there is always a driving mechanism, either SF or AGN. We have excluded our candidate fossil outflows, as they are expected not to follow a relation with AGN or SFR, although AGN variability will still be a source of scatter.

The resulting best fit is

$$\log(\dot{M}_{\rm outf}({\rm H_2})/({\rm M_\odot\ yr^{-1}})) = 1.14\log\Big(0.52\frac{\rm SFR}{\rm M_\odot\ yr^{-1}} + 0.51\frac{L_{\rm AGN}}{10^{43}{\rm erg\ s^{-1}}}\Big) - 0.41\log\Big(\frac{M_\star}{10^{11}{\rm M_\odot}}\Big), \quad (5)$$

with one standard deviation errors on the four parameters being $\Delta(x,\alpha,\beta,y) = (0.12,0.19,0.25,0.25)$. The resulting relation is shown in Fig. 10. Clearly, the large dispersion seen in the previous plots (outflow rate versus $L_{\rm AGN}$, versus SFR and versus $M_\star$ separately) is greatly reduced in this relation, indicating that we are simultaneously capturing the contribution of these three factors to the outflow rate. Very interestingly, this relation enables us to disentangle (at least partly) the contribution of the three factors to the outflow rate. The dependence on stellar mass is now seen more clearly: the dependence has a power-law index of –0.41, which is very close to the value expected by theory of –0.5 for outflows driven by star formation. As our sample also includes AGN-driven outflows, it is likely that these have mass-loading factors that decrease with stellar mass, too. We cannot disentangle in this kind of analysis the power-law index of the dependence on AGN luminosity and SFR separately. With the functional form adopted by us the combined dependence has a power-law index of 1.1, i.e. a nearly linear relation, as expected in many models at least for the SFR.

However, this relation only accounts for the molecular phase of the outflow. As discussed in Section 3.1, including the atomic-neutral and ionized phases is difficult because we do not have enough statistics in terms of galaxies that have all three outflow phases measured. However, as mentioned in Section 3.1, we can roughly account for these two phases by including a factor of 3 for star-forming galaxies (as they have an ionized and atomic outflow rates that are similar to the molecular outflow rate) and a factor of 2 for AGN-dominated galaxies (as they have an atomic outflow rate similar to the molecular outflow rate and a negligible contribution from the ionized outflow rate, at least in our luminosity range). In this case, the resulting best fit for the *total* outflow rate is given by

$$\log(\dot{M}_{\rm outf}({\rm tot})/({\rm M_\odot\ yr^{-1}})) = 1.13\log\Big(1.29\frac{\rm SFR}{\rm M_\odot\ yr^{-1}} + 0.81\frac{L_{\rm AGN}}{10^{43}{\rm erg\ s^{-1}}}\Big) - 0.37\log\Big(\frac{M_\star}{10^{11}{\rm M_\odot}}\Big), \quad (6)$$

with one standard deviation errors on the four parameters being $\Delta(x,\alpha,\beta,y) = (0.55, 0.45, 0.12, 0.24)$. The resulting fit is shown in Fig. 11, which has a scatter even smaller than in Fig. 10.

These *global* relations can be used to infer the expected outflow rate in any kind of galaxies, and provide an appropriate comparison for the theoretical models and simulations.

3.2.4 Dependence on L_{AGN}/L_{Edd}

In the previous subsections, we have investigated the dependence on nuclear activity in terms of AGN absolute luminosity. However, both in energy-driven outflows and radiation pressure-driven out-

flows (the two main mechanisms proposed for AGN outflows), the most fundamental quantity is the AGN luminosity relative to the Eddington limit, L_{AGN}/L_{Edd}. This quantity is more difficult to determine as it requires an estimate of the black hole mass. The latter has been inferred only for about half of the galaxies in our sample with a variety of methods (primarily through virial estimators) and subject to large uncertainties. The major contribution to this uncertainty stems from the virial coefficient f, which shows a scatter of 0.44 (Woo et al. 2010). Fig. 12(a) shows the outflow rate as a function of Eddington ratio. If one excludes SF-dominated galaxies, which are driven by a different mechanism (see also discussion in the next sections), the plot shows some correlation between outflow rate and Eddington ratio, although with a few points subject to large scatter. Such a scatter could partly be accounted for by the uncertainties in the black hole masses. Additional discussion on this dependence will be given in Section 4.

3.2.5 Dependence on black hole mass

In Fig. 12(b), we also show the outflow rate as a function of black hole mass. In principle, one should not expect any correlation of the outflow rate with the black hole mass, but the plot clearly shows a significant correlation. Such a correlation was already identified by Rupke et al. (2017), although with lower statistics. One interpretation is that this correlation is simply a consequence of the correlation between outflow rate and stellar mass (Section 3.2.2), through the black hole–galaxy mass relation. However, another possibility is that the correlation between outflow rate and black hole mass traces the average driving effect that the black hole has during its intermitted accretion phases. Indeed, if one assumes that the black hole accretes at a given Eddington fraction L_{AGN}/L_{Edd} (e.g. at the average Eddington fraction of the AGN population) and with an average duty cycle, then the black hole mass may be a tracer of the average AGN activity over the past $\sim 10^6$–10^8 yr, i.e. on time-scales closer to the outflow dynamical time-scale, hence resulting in the observed correlation. We discuss the effects of the AGN flickering further in the next sections.

3.2.6 Dependence on radio power

Galactic outflows are seen to also be linked with the presence of radio jets. The connection appears to be common for what concerns the ionized phase of outflows (Mullaney et al. 2013). Furthermore, clear indications that some molecular and atomic outflows are associated with radio jets have been found (e.g. Morganti et al. 2013, 2015; Dasyra et al. 2015, 2016). However, it is not yet clear how common this association is among molecular outflows.

We have explored this connection in our sample by investigating the correlation of the outflow rate with the excess of radio power relative to the value expected from the radio–SFR correlation, which is traced by the parameter q_{IR}, defined as the ratio between the FIR flux and the monochromatic flux at 1.4 GHz (Section 2.4.6). Fig. 13 shows the molecular outflow rate as a function of the parameter q_{IR}. The vertical dashed line indicates the average value for star-forming galaxies, while the solid vertical line indicates the limit below which galaxies are considered to have a significant radio excess associated with a radio jet (Ivison et al. 2010; Harrison et al. 2014).

Most galaxies in our sample are consistent with the radio luminosity being associated with star formation. Actually it seems that, on average, q_{IR} in our sample is even higher than typically observed in normal galaxies, possibly reflecting the bias towards star-bursting systems, or the contribution of powerful AGN to the IR emission in some of the galaxies of our sample.

The Fig. 13 shows that two of the three galaxies with radio excess ($q_{IR} < 1.8$) do have strong outflows. However, the plot shows no clear correlation between molecular outflow rate and excess of radio emission relative to the SFR–radio relation. This finding suggests that, statistically, the presence of radio jets does not seem to be a primary driving mechanism of the majority of galactic molecular outflows in our sample. However, this does not imply that strong radio jets cannot cause outflows. In fact, as already discussed at the beginning of this section, radio jets have been seen as the origin of powerful outflows in a few specific galaxies.

3.3 Depletion time

In the following, we estimate the outflow depletion time-scale, defined as $\tau_{\rm depl,\ outf} = M_{\rm gas}/\dot{M}_{\rm outf}$, i.e. the time required to remove all gas from the galaxy with the current mass outflow rate assuming no fresh supply of additional gas is delivered to the galaxy. We first focus on the depletion time of the molecular gas, i.e. $\tau_{\rm depl,outf}(H_2) = M(H_2)/\dot{M}_{\rm outf}(H_2)$, as we have this information for all galaxies in the sample and we will then discuss the total gas depletion time for galaxies that have information on their H I content. In Fig. 14, we show the relation between molecular depletion time-scales and AGN luminosity. While we do observe an anticorrelation between depletion time-scales and AGN luminosity, and with AGN contribution to the bolometric luminosity, the trend is much more scattered than in previous studies (Sturm 2011; Cicone et al. 2014). The depletion time-scale of molecular gas for the most powerful AGN is between a few times 10^6 and 10^8 yr.

Fig. 15 shows the depletion time due to outflows compared to the depletion time-scale due to star formation. For star-forming galaxies, the depletion time due to star formation is similar or shorter than the depletion time due to outflowing gas. For AGN hosts, the depletion is dominated by outflows rather than by gas consumption due to star formation, implying that AGN-driven outflows play a key role in regulating star formation in galaxies.

For about half of the galaxies, we also have information on the atomic gas content, hence we can estimate the total depletion time: $\tau_{\rm depl}({\rm tot}) = M(H_2 + {\rm H\,I})/\dot{M}_{\rm outf}(H_2)$. This is shown in Fig. 16, which illustrates that the total depletion time-scale is much longer, and generally exceeding 10^8 yr even in most AGN (even if the other gas phases are included, as shown by the black arrow), implying that the AGN is unlikely to clear the galaxy of its total gas content.

The combination of these various results indicates that AGN-driven outflows are capable of clearing the central parts of galaxies, where the gas content is dominated by the molecular phase, but the AGN is unlikely to clear the entire galaxy of its gas content.

3.4 Kinetic power

It is important to investigate the properties of outflows such as their kinetic power and momentum rate, as different models make different predictions for these quantities. In this section, we briefly discuss the observational results for what concerns the kinetic power; in the next section, we will discuss the momentum rate, while a detailed analysis of implications and comparison with models will be given in Section 4.1.

Fig. 17 shows the kinetic power of the outflow ($= 0.5\ v^2 \dot{M}_{\rm outf}$) as a function of the radiative power of the AGN. Clearly, for AGN host galaxies the kinetic power correlates with the AGN luminosity, although the correlation appears to be superlinear. Moreover, our

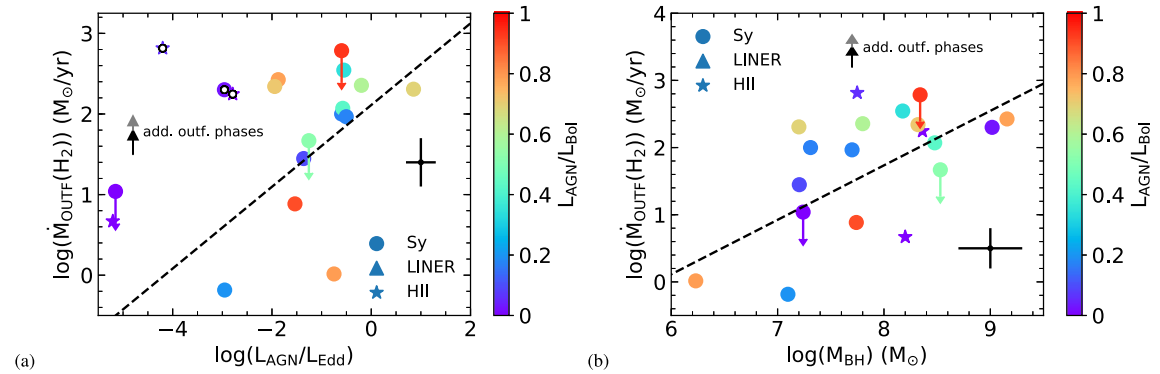

Figure 12. Outflow rate as a function of Eddington ratio, i.e. L_{AGN}/L_{Edd}. Outflow rate as function of black hole mass. Colour-coding and symbols are same as in Fig. 2.

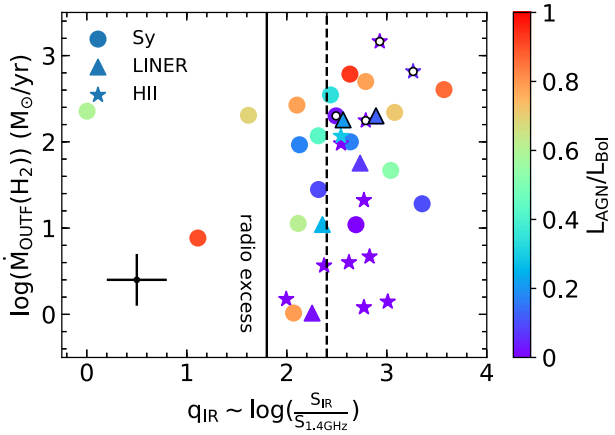

Figure 13. Molecular outflow rate as a function of the parameter q_{IR} defined as the ratio between the FIR flux and the radio monochromatic flux at 1.4 GHz (Section 2.4.6). The vertical dashed line indicates the average value for star-forming galaxies, while the solid vertical line indicates the limit below which galaxies are considered to have a significant radio excess associated with a radio jet (Ivison et al. 2010; Harrison et al. 2014). Colour-coding and symbols are same as in Fig. 2.

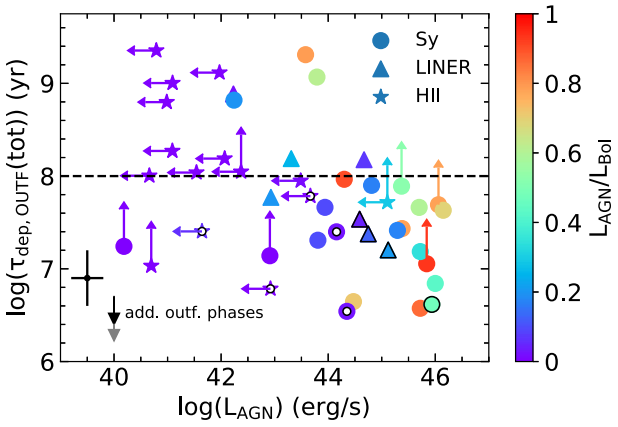

Figure 14. Molecular gas depletion time-scale due to outflows as a function of AGN luminosity. Colour-coding and symbols are same as in Fig. 2.

more extended, and less biased sample, with respect to previous studies, reveals a large scatter.

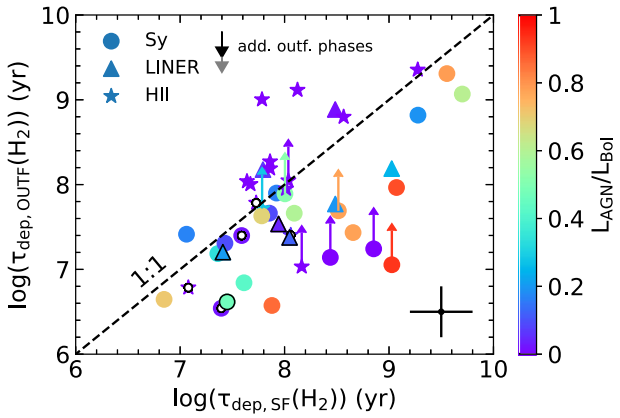

Figure 15. Molecular gas depletion time-scale due to outflows versus depletion time-scale due to star formation. Colour-coding and symbols are same as in Fig. 2.

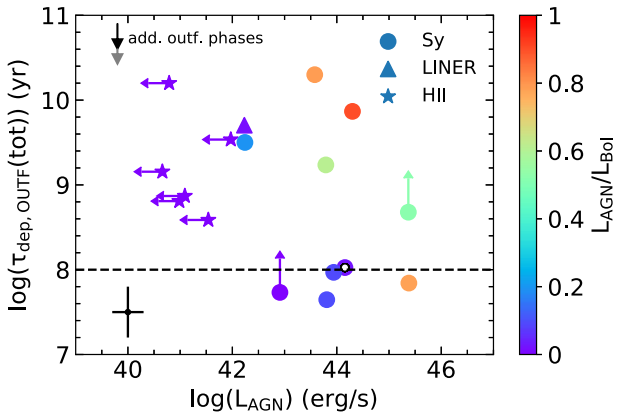

Figure 16. Total gas (H I + H_2) depletion time-scale as a function of AGN luminosity. Colour-coding and symbols are same as in Fig. 2.

Star-forming galaxies follow different relations compared to AGN, as expected since in these sources the observed outflows cannot have originated from a currently active AGN episode. To test whether star formation can explain why these galaxies are outliers, in Fig. 18 we compare the kinetic power of the outflow with the power expected to be generated by SNe ($P_{K,SF} = 7 \times 10^{41}$ SFR ($M_\odot$ yr^{-1}) (Veilleux, Cecil & Bland-Hawthorn 2005). In star-forming galaxies, especially those with low values of $P_{K,SF}$, the

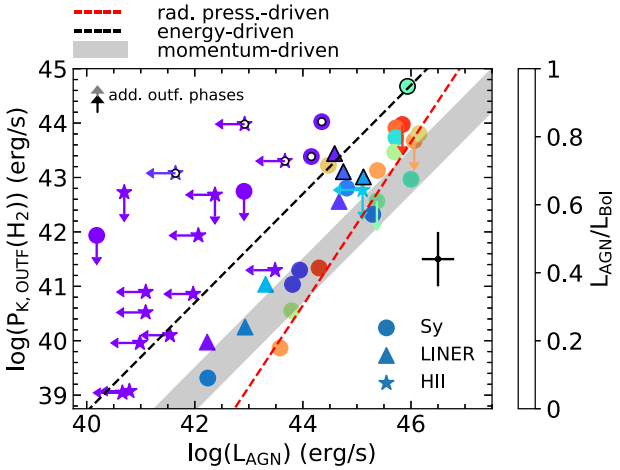

Figure 17. Kinetic power ($P_{\rm K,\,outf}$) of the outflow as a function of the AGN luminosity. The dashed black line indicates the theoretical prediction of $P_{\rm K} = 0.05 L_{\rm AGN}$ for an energy-driven outflow, assuming a coupling efficiency of 100 per cent between the outflow and the ISM. The prediction for momentum-driven outflows and some radiation pressure-driven outflows is shown as a shaded region. The red dashed line shows the predicted relation for the radiation pressure-driven outflow presented in Ishibashi, Fabian & Maiolino (2018). Colour-coding and symbols are same as in Fig. 2.

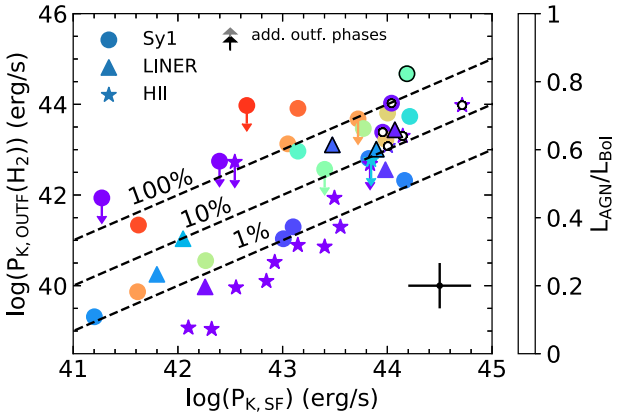

Figure 18. Kinetic power of the outflow as a function of the kinetic power generated by SNe, as inferred from the SFR. The black dashed lines indicate coupling efficiencies of 1, 10, and 100 per cent. Colour-coding and symbols are same as in Fig. 2.

kinetic power of the outflow can be explained by SNe by assuming a coupling efficiency of only 0.5 per cent (except for a few SF galaxies with extreme outflows discussed further below). However, accounting for the contribution of the ionized and atomic phases increases the kinetic power of SB-dominated outflows by a factor of ∼3 (Section 3.1), as indicated by the grey arrow, suggesting a coupling efficiency of SN ejecta with the ISM higher than 1 per cent. Conversely, in AGN host galaxies a coupling of ∼10 per cent or much more is needed; as this is significantly larger than expected by models of SN outflows (especially if accounting for the other outflow phases, as indicated with the black arrow), this indicates, as expected, that SNe are not powerful enough to drive the outflow in these objects and that the outflow must be mostly driven by the AGN.

Figs 17 and 18 also clearly indicate that there are a few galaxies for which the kinetic power greatly exceeds what expected from

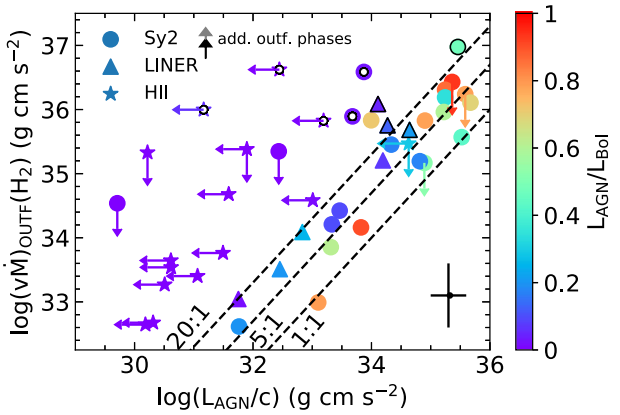

Figure 19. Relation between outflow momentum rate ($v_{\rm outf}\dot{M}_{\rm outf}({\rm H_2})$) and AGN radiative momentum rate ($L_{\rm AGN}/c$). The theoretical predictions $(v_{\rm outf}\dot{M}_{\rm outf})/(L_{\rm AGN}/c) \sim 20{:}1$ (energy driven) and 1:1 (momentum driven) are shown as a dashed lines, respectively. Radiation pressure-driven outflows can reach $(v_{\rm outf}\dot{M}_{\rm outf})/(L_{\rm AGN}/c) \sim 5{:}1$. Colour-coding and symbols are same as in Fig. 2.

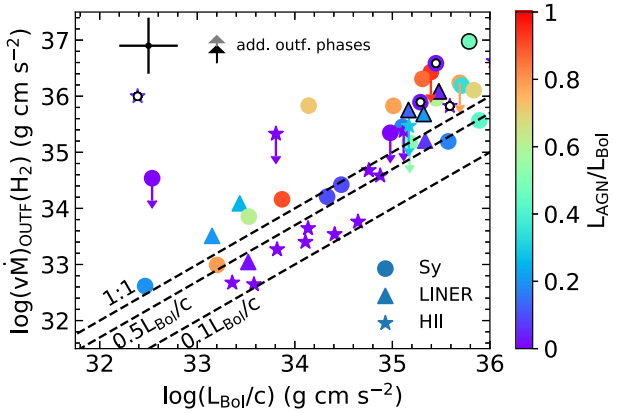

Figure 20. Dependence of the outflow momentum rate ($v_{\rm outf}\dot{M}_{\rm outf}$) on the total photon momentum output of the galaxy (i.e. from AGN *and* star formation). The top dashed line indicates the 1:1 relation between momentum rate and bolometric luminosity, while lower dashed lines indicate lower ratios. Colour-coding and symbols are same as in Fig. 2.

the AGN energy-driven scenario and also in excess of what is expected by the SNe-driven scenario, as a coupling efficiency higher than 10 per cent would be required. In these cases (objects marked by white dot in their centre), the outflow is likely due to a past, more active phase of the AGN. This will be discussed further in Section 4.3.

3.5 Momentum rate

The outflow momentum rate is plotted as a function of the AGN radiative momentum rate $L_{\rm AGN}/c$ in Fig. 19, illustrating a good correlation of these two quantities for AGN host galaxies, further indicating that AGN play a significant role in driving galactic outflows. However, also in this case it is clear that the scatter is significantly larger than in previous studies.

Galaxies classified as star forming are all outliers in this relation since they are powered by a different mechanism (i.e. SNe feedback and/or radiation pressure from the stellar UV radiation field). In Fig. 20, we analyse the dependence of outflow momentum rate on

total photon momentum rate of the galaxy, $L_{\rm bol}/c$. For strong AGN hosts, $L_{\rm bol} \approx L_{\rm AGN}$, but for AGN with lower AGN contribution and star-forming galaxies, $L_{\rm bol}$ is much larger than $L_{\rm AGN}$. In this plot, it is interesting to note that for some star-forming galaxies, especially at high luminosities (i.e. high SFR) the momentum rate is close to $\sim$0.5 $L_{\rm bol}/c$, suggesting that radiation pressure on dusty clouds by the radiation field of young stars can be an additional significant contributor to the driving mechanism of outflow in starburst galaxies, as predicted by some models (Thompson et al. 2015), although a coupling efficiency of at least 50 per cent would be required.

In some star-forming galaxies, the momentum rate of the outflow is close or exceeding $L_{\rm bol}/c$ (which would imply an unrealistic coupling efficiency of 100 per cent or higher), indicating that other mechanisms or other phenomena may be at work. This is also seen in some AGN: A few AGN hosts have outflows which, when compared with $L_{\rm AGN}/c$, are characterized by momentum boosts well in excess of what expected by any theory (see Fig. 19). As we will discuss later on, most of these outflows with extreme momentum rates can be explained in terms of fossil outflows resulting from a much stronger past AGN activity.

4 DISCUSSION

4.1 Driving mechanisms in AGN

Three different mechanisms have been proposed for powering AGN-driven outflow: an energy conserving blast wave (so-called energy-driven), a momentum conserving blast wave (so-called momentum-driven), and direct radiation pressure on to the dusty clouds of the galactic ISM (so-called radiation pressure-driven). These are discussed in greater detail in the following.

Many theoretical models expect that the most effective feedback process is obtained through AGN-driven outflows that are energy conserving (energy-driven), in which a hot bubble composed of a thermalized nuclear wind has a cooling time-scale much longer than the outflow expansion time-scale. The outflow is accelerated due to the adiabatic expansion of the hot bubble. In this scenario, the outflow kinetic energy is expected to be about 5 per cent of the AGN radiative power, if the AGN is accreting close to the Eddington limit and if a 100 per cent thermal-to-kinetic conversion efficiency and high gas covering fractions are assumed (i.e. 100 per cent coupling between the blast wave and the ISM in the host galaxy) (King 2010; Faucher-Giguere & Quataert 2012; Zubovas & King 2012; Costa, Sijacki & Haehnelt 2014; King & Pounds 2015; Richings & Faucher-Giguère 2018). Yet, more detailed 3D, non-spherically symmetric simulations have suggested that the coupling can be significantly lower than 100 per cent, with dense clumps of the ISM remaining unaffected and the outflow escaping along the directions of least resistance (Bourne, Nayakshin & Hobbs 2014; Gabor & Bournaud 2014; Bourne, Zubovas & Nayakshin 2015; Costa, Sijacki & Haehnelt 2015; Roos et al. 2015).

Momentum-driven outflows (in which the energy of the shocked wind is quickly dissipated on small scales via radiation losses) are generally expected to be much less effective in driving outflows and in this case the outflow kinetic energy is expected to be of the order of 0.1 per cent of the AGN radiative luminosity, or less (King & Pounds 2015). Momentum-driven outflows are also expected to be confined within the central few 100 pc as most of their energy is quickly dissipated.

An additional class of models suggests that direct radiation pressure of the UV, optical, and IR photons on the dusty clouds of the ISM can be effective enough to drive massive outflows (Fabian 2012; Thompson et al. 2015; Bieri et al. 2017; Ishibashi, Banerji & Fabian 2017; Costa et al. 2018a; Costa et al. 2018b; Ishibashi et al. 2018). In this case, there is a broad range of expected outflow properties. If the central dusty region in which acceleration takes place is optically thick to IR radiation, then the kinetic power of the outflows can be as high as $\sim$1 per cent of the AGN luminosity (this applies also when the source of radiation is a compact starburst); however, in less extreme cases, the outflow kinetic power is expected to be lower than this value. Recently, Ishibashi et al. (2018) developed the model of radiation pressure-driven outflows further. They predict a superlinear relation between outflow kinetic power and AGN luminosity in the form $P_{\rm K,\,outf} \propto L_{\rm AGN}^{3/2}$.

By looking at the results reported in Section 3.4 and Fig. 17, where the prediction of different models are also shown, it is clear that outflows in AGN host galaxies span a broad range of properties. Although AGN 'flickering' can account for some of the scatter, as discussed in the next section, the very broad range of $P_{\rm K,\,outf}/L_{\rm AGN}$ suggests that these outflows are driven by a combination of different driving mechanisms and/or a broad range of coupling efficiencies with the ISM. Some AGNs are consistent with the energy-driven scenario, and full coupling of the outflow with the ISM. However, the majority of AGNs are significantly below the $P_{\rm K} = 0.05 L_{\rm AGN}$ relation (which assumes all thermal energy of the putative expanding hot bubble is converted into kinetic energy of the outflow) and so the respective outflows are more consistent with a momentum-driven or radiation pressure-driven mechanism; alternatively, they are energy-driven, but poorly coupled with the galaxy ISM. However, the momentum-driven scenario can probably be excluded as the observed outflows are mostly on kpc-scales, while momentum-driven outflows should be confined within the central few 100 pc (King & Pounds 2015).

As shown in Fig. 17, at high AGN luminosities, galaxies lie closer to the expected value for the energy-driven mode though still mostly below the value expected from energy-driven outflows. This seems to indicate that different driving mechanisms may be at work at different luminosities. Specifically, at high luminosities energy-driven outflows (though with poor coupling) may dominate, while at low luminosities radiation pressure may be the dominant mechanism driving outflows.

The superlinear relation between outflow kinetic power and AGN luminosity in the form $P_{\rm K,\,outf} \propto L_{\rm AGN}^{3/2}$ expected by the radiation pressure model of Ishibashi et al. (2018) (dashed orange line in Fig. 17) is consistent with the observed relation in terms of slope. Therefore, this model can potentially account also for the high $P_{\rm K,\,outf}/L_{\rm AGN}$ values ($\sim$1 per cent) observed at the highest luminosities, and the decreasing values of this ratio at lower luminosities. However, the model also expects the outflow rate to follow a relation $\dot{M}_{\rm outf} \propto L_{\rm AGN}^{1/2}$, which is somewhat shallower than what we observe for molecular gas (see Fig. 7).

In terms of momentum rate, in the energy-driven case models expect that the momentum rate is boosted to about 15–20 $L_{\rm AGN}/c$ (Faucher-Giguere & Quataert 2012; Zubovas & King 2012). Momentum-driven winds are expected to result in momentum rates of $\sim L_{\rm AGN}/c$ (King 2010). Direct acceleration of the ISM through the action of radiation pressure on dusty clouds generates momentum rates ranging from $\sim$1 up to 5 $L_{\rm AGN}/c$, the latter in the case that the medium that is being accelerated is optically thick to IR radiation, resulting in multiple scattering that boosts the momentum rate (Ishibashi & Fabian 2015; Thompson et al. 2015; Bieri et al. 2017; Costa et al. 2018b; Ishibashi et al. 2018).

In Fig. 19, the upper dashed line represents the theoretical prediction for the energy-driven model (with 100 per cent coupling),

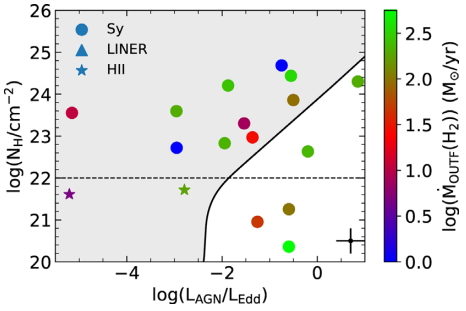

Figure 21. Gaseous column density along our line of sight, as inferred from X-ray spectra, versus L_{AGN}/L_{Edd}, with symbols colour-coded by outflow rate (right-hand side colour bar). The solid line delimitates the area (non-shaded) where radiation pressure on dust is expected to overcome gravity (i.e. where the effective Eddington luminosity for a dusty medium is exceeded) hence producing powerful outflows. Symbols are same as in Fig. 2.

while the lower dashed lines indicate the values expected for the momentum-driven and radiation pressure-driven models. Some of the galaxies with an AGN do follow the theoretical prediction for energy-driven outflows within the errors, but most galaxies hosting an AGN have momentum rates scattered between the energy-driven case and the momentum/radiation pressure-driven cases, further suggesting the contribution of different driving mechanisms and/or energy-driven outflows with poor coupling.

An additional route to study the driving mechanism is to investigate the relation between outflow rate, AGN luminosity and gas column density of the circumnuclear gas. Indeed, in the context of radiation pressure-driven outflows, the effective Eddington luminosity is dominated by radiation pressure on dust, which drastically reduces the Eddington limit. Fabian, Vasudevan & Gandhi (2008) and Ricci et al. (2017) have pointed out that the effective Eddington limit ($L_{Edd,\,eff}$) is higher at higher gas column densities as larger amounts of material need to be pushed out. Hence, these authors expect a region in the L_{AGN}/L_{Edd} versus N_H plane where radiation pressure on dust dominates over gravity and where this kind of outflows should be most effective. This is explored in Fig. 21, where the column density (as inferred from X-ray observations) is shown as a function of the Eddington ratio, L_{AGN}/L_{Edd}, and colour-coding is according to the outflow rate. The region on the right-hand side of the plot, delimited by the solid line, is where the effective Eddington luminosity for a dusty medium is exceeded, and therefore where we expect powerful outflows that are driven by radiation pressure on dust. As pointed out by Fabian et al. (2008) and Ricci et al. (2017), this region is underpopulated, indeed empirically confirming that the effective Eddington ratio is exceeded in this region. The few galaxies of our sample located in this region do indeed show among the highest outflow rates, suggesting that indeed these extreme outflows may be driven by radiation pressure on dust. We note that in the scenario discussed by Fabian et al. (2008) and Ricci et al. (2017), AGNs with $N_H < 10^{22}$~cm^{-2} are not considered, as these low column densities are thought to be associated with dust lanes in the host galaxy and not directly linked with the AGN process; however, our analysis shows that the three objects in this region are characterized by strong outflows, suggesting that also in these cases the outflow is driven by radiation pressure on dust. For the other galaxies, located on the left-side of the solid line (shaded are) there is not much correlation between the outflow rate and their location on the diagram, in particular there are galaxies with high outflow rates also below the boundary expected by the model. These outflows could be driven by a different mechanism.

To summarize, our results indicate that AGN-driven outflows are either consistent with predictions from direct radiation pressure models or with the energy-conserving blast-wave scenario, but with a coupling with the ISM of the host galaxy that varies from galaxy to galaxy and generally is lower than 100 per cent.

4.2 Driving mechanisms in star-forming galaxies

As discussed in Section 3.4 only about ∼1–2 per cent of the kinetic power released by SNe appear to be converted into outflow kinetic power. A low coupling efficiency of the kinetic energy between SN ejecta and ISM is expected by the fact that most of the energy is radiated away in the dense interstellar medium in which most SNe are expected to explode. Yet, models and simulations expect still higher coupling efficiencies, of the order of 5 per cent (Walch & Naab 2015). Although, there is some tension this is actually within the errors; however, if confirmed with more accurate data it may indicate that radiation losses during the SN–ISM interaction are higher than expected (possibly because the ISM is denser than assumed in the simulations).

However, in addition to the kinetic power injected by SNe, outflows in star-forming galaxies can also be driven by radiation pressure on to the dusty clouds (Thompson, Quataert & Murray 2005; Thompson et al. 2015). The correlation in Fig. 20 between outflow momentum rate and radiative momentum from the bolometric luminosity of star-forming galaxies suggests indeed that radiation pressure may play a role. However, one should also be aware that such a correlation is also degenerate with the kinetic power injected by SNe, since the SN rate is linked to the SFR which is in turn related to the bolometric luminosity. Moreover, it is important to note that most star-forming galaxies have a ratio between momentum rate and radiation momentum is between 0.5 and 0.1 (Fig. 20), implying that, if this driving process is at work, the coupling efficiency must be less than 50 per cent.

4.3 Fossil outflows

There are a few galaxies with outflows that are characterized by anomalously high kinetic power and momentum rates compared to their AGN luminosity and SFR, which are difficult to explain with any driving mechanism. More specifically, Figs 17 and 18 indicate that for some galaxies (marked with a white dot in these and other figures) the kinetic power is greatly in excess of what is expected even from the AGN energy-driven scenario, even assuming 100 per cent coupling, and is also in excess of what is expected by the SNe-driven scenario, unless assuming an unrealistically high coupling efficiency of the SNe (larger than 10 per cent, especially if accounting for all outflow phases). In Fig. 19, it is clear that these objects have also very high momentum rate, even in excess of what expected in the case of energy-driven outflows and 100 per cent coupling. It is unlikely that in these objects the SFR or AGN power is not estimated properly, as the observational constraints are quite good. It is also unlikely that these outflows are driven by a radio-jet, as these objects do not show any radio excess in Fig. 13. In these cases, as already hinted in the previous sections, the most likely explanation is that we are observing 'fossil' outflows that outlast a past powerful AGN activity, which has recently faded. This interpretation is further supported by the low Eddington ratios ($\log(L_{AGN}/L_{Edd}) \lesssim -3$) seen in the three fossil outflow objects for which a black hole estimate is available.

Fossil outflows are expected from theory in large numbers. It has been shown that outflows can remain visible for a time about 10 times longer than the driving phases and up to 10^8 yr (King, Zubovas & Power 2011). Theoretical considerations have suggested that in M82 a powerful AGN might have been present until about 17 Myr ago and may have been responsible for driving the outflow currently observed (Zubovas 2015). Even more simply, without invoking detailed and extensive theoretical simulations, the dynamical time-scales of the outflows ($t_{\rm dyn} \sim R/v$) are in the range of 10^6–10^8 yr, while we know that AGNs have a 'flickering' time-scale ranging from a few years (e.g. Gilli et al. 2000) up to 10^5 yr (King & Nixon 2015; Schawinski et al. 2015). Therefore, a large number of fossil AGN is naturally expected. The outliers we see here are possible manifestations of this scenario and are likely the tip of the iceberg of a much larger population of fossil outflows. If this is true, then one should be careful when comparing observational outflow properties with theoretical models as possibly a large fraction of galaxies (in our sample 10–20 per cent) display fossil outflows.

The reason why in the past such fossil outflows had not been identified is likely because previous observations had targeted primarily known, strong AGN hence biasing the sample towards outflows that are in the phase of being powered. Instead, in our study we have collected data of galaxies from the ALMA archive, many of which had been observed independently of their activity, hence reducing such biases.

Table 3 gives the list of fossil outflows identified by us. Their properties have no peculiarities relative to other galaxies in the sample.

4.4 Do outflows escape the galaxy and the halo?

If outflow velocities are high enough to escape the potential of the galaxy (and possibly even the halo), then these outflows can effectively clear the galaxy of its gas content. It also depends on how much gas the outflows sweep up as they move out of the galaxy and on whether they collide with inflowing material. We ignore the latter effects here, because, as it turns out, most outflowing material should not escape the galactic halo purely due to its insufficient velocity. Mass-loading and a potential interaction with gas infall would only strengthen our conclusions.

In principle, one should use the velocity rotation curve of galaxies to infer the mass distribution radial profile of the associated gravitational potential. Unfortunately, at the moment, this information is not available for the vast majority of the galaxies in our sample. Information on the rotation curve is available only for very few galaxies, primarily from the CO interferometric data, and only in the central region of the galaxy. As a consequence, we have to rely on some simple assumptions and use scaling relations with the stellar mass.

We consider the stellar mass as determined in Section 2.4. We use the relation by McIntosh et al. (2005) at $z = 0$ to relate the stellar mass to the half-light radius r_{50}:

$$\log(\bar{r}_{50}/{\rm h}^{-1}{\rm kpc}) = 0.56 \log(M_\star {\rm h}^2/{\rm M}_\odot) - 5.52. \quad (7)$$

We approximate the stellar mass distribution adopting a Hernquist profile (Hernquist 1990) for the density

$$\rho(r) = \frac{M}{2\pi}\frac{a}{r}\frac{1}{(r+a)^3}, \quad (8)$$

where a is related to the effective radius $r_{\rm eff}$ via $r_{\rm eff} \approx 1.8135a$. We can now compute the escape velocity for galaxies in our sample. The escape velocity is given by

$$v_{\rm esc} = \sqrt{2|\Phi(r)|} = \sqrt{\frac{2GM}{r+a}}. \quad (9)$$

The escape fraction is then defined as the fraction of the outflow that has a velocity higher than the escape velocity. Unfortunately, this calculation can be done only for those outflows for which we have the data in electronic form, as it requires estimating the integral of the fraction of the broad wings with velocity higher than the escape velocity (i.e. this calculation cannot be done for the data in the literature for which an electronic version of the spectrum is not available). This part of the outflow will eventually leave the galaxy. In Fig. 22, the escape fraction is shown for the galaxies as a function of the AGN luminosity. Only in IRAS 20100–4156, and maybe in 4C 12.50, 10 per cent or more of the gas in the outflow will escape the galaxy using these simple assumptions. For all other galaxies, the escape fraction is smaller or negligible and there is no clear dependence on AGN luminosity. We should note, however, that the equations here only hold if we consider ballistic motions. If the outflows are still driven and therefore further accelerated, they are more likely to escape the galaxy potential. The error in the escape fraction is as large as 50 per cent as inferred by running a Monte Carlo simulation, taking into account errors in fitting the line profile, stellar mass, and outflow radius.

Therefore, despite galactic outflows being very massive and energetic, especially those driven by AGN, most of the expelled gas will quickly re-accrete on to the galaxy and be available again for star formation. Hence, the ejection of gas, at least in this molecular phase, does not really contribute to the global quenching of star formation in galaxies. However, these outflows can still have a dramatic effect in the central region of galaxies (especially in the bulge region), where they can locally suppress or even quench star formation. Moreover, even if the ejective aspect of outflows does not directly contribute to the global quenching of galaxies on large galactic scales, this does not mean that outflows do not play a role at all on the global evolution of galaxies on large scales. By injecting energy, outflows can keep the halo gas hot and prevent it from cooling on to the galaxy, hence effectively resulting into a delayed quenching of star formation in the galaxy as a consequence of starvation (e.g. Costa et al. 2018a; Gilli et al. 2017). The escape fractions inferred above are for molecular outflows. Ionized outflows, although generally contributing much less to the outflow rate, are expected to have higher escape fractions (Costa et al. 2015). This can be investigated for several galaxies whose outflow has been mapped in the ionized phase, but we defer this kind of analysis to a later paper.

We note that the escape fraction discussed above refers to the escape velocity from the galaxy. The escape fraction from the galaxy dark matter halo are even smaller, but also more difficult to compute. We can attempt to estimate the velocities needed to escape the halo by making a few approximations in the following.

We use the Navarro–Frenk–White (NFW) profile (Navarro, Frenk & White 1995) to describe the density in the halo of the galaxy:

$$\rho(r) = \frac{\rho_{\rm crit}\delta_{\rm c}}{r/r_{\rm s}(1+r/r_{\rm s})^2}, \quad (10)$$

where $\rho_{\rm crit} = 3H^2/8\pi{\rm G}$ is the critical density and $r_{\rm s} = r_{200}/c$ is the characteristic radius (c being the concentration parameter). The mass of the halo (M_{200}) can be inferred from the stellar mass using a stellar mass–halo mass relation from abundance matching (Moster, Naab & White 2013). To find the mass concentration from the halo

Table 2. Outflow properties of the sample.

Galaxy	log $M_{\rm outf}(H_2)$ ($M_\odot$)	$R_{\rm outf}$ (pc)	$v_{\rm outf}$ (km s^{-1})	$\dot{M}_{\rm outf}(H_2)$ ($M_\odot$ yr^{-1})	log $\tau_{\rm depl,outf}(H_2)$ (yr)	$\frac{P_{\rm K,outf}(H_2)}{L_{\rm AGN}}$	$\frac{\dot{M}_{\rm outf}(H_2)v}{L_{\rm AGN}/c}$	$\dot{M}_{\rm outf}$(ion) ($M_\odot$ yr^{-1})	$\dot{M}_{\rm outf}$(HI)$_{\rm NaID}$ [$M_\odot$ yr^{-1}]	$\dot{M}_{\rm outf}$(HI)$_{\rm [CII]}$ [$M_\odot$ yr^{-1}]	ef. [%]	Ref.	Trans.
(1)	(2)	(3)	(4)	(5)	(6)	(7)	(8)	(9)	(10)	(11)	(12)	(13)	(14)
Literature data													
IRAS F08572 + 3915	8.61	820	800	403	6.57	0.016	11	0.32	25	130		(a)	1-0
IRAS F10565 + 2448	8.37	1100	450	100	7.90	0.0010	13	0.54	65	180		(a)	1-0
IRAS 23365 + 3604	8.17	1230	450	57	8.18	0.008	10					(a)	1-0
Mrk 273	8.24	550	620	200	7.40	0.17	160	0.66	7.9	110		(a)	1-0
IRAS F23060 + 0505	≤9.56	≤4050	(550)	≤500	≥7.69	≤0.004	≤4.5					(a)	1-0
Mrk 876	≤9.48	≤3550	(700)	≤610	≥7.05	≤0.014	≤12					(a)	1-0
I Zw 1	≤7.67	≤500	(500)	≤47	≥7.90	≤0.0016	≤1.9					(a)	1-0
Mrk 231	8.47	600	700	350	7.19	0.01	8.8	0.05	180	250	4.6	(a)	1-0
NGC 1266	7.93	450	177	11	8.19	0.005	18				2∗	(a)	1-0
M82	8.08	800	100	4	8.04	≥0.036	≥218					(a)	1-0
NGC 1377	7.29	200	110	5	7.77	0.0021	11				<1	(a)	2-1
NGC 6240	8.61	650	400	267	7.43	0.006	8.4			≤1300		(a)	1-0
NGC 3256	7.34	500	250	4	9.12	≥0.08	≥190	3.6	26			(a)	2-1
NGC 3628	7.36	400	50	1.5	9.35	≥0.019	≥230					(a)	1-0
NGC 253	6.32	200	50	1.4	8.00	≥0.024	≥290	0.60				(a)	2-1
NGC 6764	6.52	600	170	1	8.89	0.006	20					(a)	1-0
NGC 1068	7.26	100	150	28	7.66	0.0023	9.1					(a)	2-1
IC 5063	7.37	500	300	8	7.97	0.0011	2.2	0.21				(a)	2-1
NGC 2146	7.68	1550	150	5	8.27	≥0.27	≥1100					(a)	1-0
IRAS 17208 − 0014	7.66	160	600	176	7.78	≥0.43	≥430	46	34			(b)	2-1
NGC 1614	7.51	560	360	21	8.19	≥0.74	≥1200	13	22			(b)	1-0
Circinus Galaxy	6.48	450	150	1	9.31	0.0002	0.78	0.07				(c)	1-0
SDSS J1356 + 1026	7.84	300	500	118	6.84	0.0009	1.1	2.7				(d)	3-2
ESO 320-G030	6.81	2500	455	1.2	9.00	≥0.63	≥840	1.6	24			(e)	2-1
NGC 1808	7.48	1000	98	3	8.80	≥0.094	≥580					(f)	1-0
NGC 1433	5.81	100	100	0.7	8.82	0.0012	7.1	0.07				(g)	3-2
M51	6.61	37	100	11	9.07	0.0006	3.5					(h)	1-0
4C 12.50	7.72	150	640	227	7.66	0.006	5.5				<30∗	(i)	3-2
IRAS 05081 + 7936	≤8.01	≤500	(400)	≤95	≥8.05							(j)	1-0
IRAS 10035 + 4852	≤8.15	≤500	(400)	≤117	≥7.72							(j)	1-0
IRAS F11119 + 3257	9.14	7000	1000	203	7.63	0.0046	2.7				5.7	(k)	1-0
ALMA archival data													
IRAS 20100-4156	9.31	663	456	1457	6.78	≥11	≥15000	2.5			9.3	(l)	1-0
PG 0157 + 001	8.39	729	268	93	7.41	0.001	2.4				0.94	(l)	3-2
IRAS 15115 + 0208	8.82	1174	103	59	7.95	≥0.006	≥38				<1	(l)	1-0
IRAS 05189 − 2524	8.87	189	491	219	6.64	0.060	69	7.0		480	7.6	(l)	3-2
NGC 4418	7.90	569	134	19	7.31	0.0017	7.6				<1	(l)	2-1
IRAS 13120 − 5453	8.55	179	549	1115	6.54	0.47	520			680	0.82	(l)	3-2
IRAS 22491 − 1808	8.73	202	241	654	7.40	≥27	≥68000				0.29	(l)	2-1
NGC 1386	≤6.23	80	500	≤17	≥7.24	≤56	≤68000					(l)	1-0
NGC 6810	≤7.20	120	500	≤64	≥7.03	≤107	≤130000					(l)	1-0
NGC 5643	≤6.92	60	500	≤85	≥7.14	≤0.68	≤820					(l)	1-0
OH outflows (González-Alfonso et al. 2017)													
IRAS F03158 + 4227	8.70	335	1000	1500	6.62	0.055	33					(m)	
IRAS F14348 − 1447	8.62	355	450	420	7.54	0.07	95			≤1500		(m)	
IRAS F14378 − 3651	8.07	255	425	180	7.20	0.008	11					(m)	
IRAS F20551 − 4250	8.00	175	450	200	7.37	0.023	31	0.40				(m)	

Notes. Outflow properties: (1) galaxy name, (2) outflow mass, (3) outflow radius, (4) outflow velocity (following the prescription in Rupke et al. (2005a)), (5) outflow mass rate, (6) depletion time due to outflows, (7) kinetic power divided by AGN luminosity, (8) momentum rate boost, (9) ionised outflow mass rate, (10) neutral outflow rate using Na I D absorption, (11) neutral outflow rate using [CII], (12) fraction of the outflowing gas escaping the galaxy (∗these values are taken from the literature and their definition of outflow velocity is slightly different from the one used here), (13): references: (a) Cicone et al. (2014), (b) García-Burillo et al. (2015), (c) Zschaechner et al. (2016), (d) Sun et al. (2014), (e) Pereira-Santaella et al. (2016), (f) Salak et al. (2016), (g) Combes et al. (2013), (h) Querejeta et al. (2016), (i) Dasyra et al. (2014), (j) Leroy et al. (2015), (k) Veilleux et al. (2017), (l) this work, includes information about which CO transition is used (m): González-Alfonso et al. (2017), (14) CO transition used for calculation of outflow properties.

mass, we use the relation by Duffy et al. (2008) at $z = 0$:

$$\log c_{200} = 0.76 - 0.1 \log M_{200}. \quad (11)$$

As in Section 4.4, the escape velocity is

$$v_{\rm esc} = \sqrt{2|\Phi(r)|} = \sqrt{\frac{2M_{200}G}{r(\ln(1+c) - c/(1+c)}\ln(1 + r/r_{\rm s}))}. \quad (12)$$

Table 3. Fossil Outflow candidates.

Galaxy	$P_{K,outf}(H_2)/L_{AGN}$	$(\dot{M}_{outf}(H_2)v)/(L_{AGN}/c)$	$P_{K,outf}(H_2)/P_{K,SF}(H_2)$ (per cent)
Mrk 273	0.17	160	27
IRAS 17208 − 0014	≥0.43	≥430	14
IRAS 20100 − 4156	≥11	≥15000	18
IRAS 13120 − 5453	0.47	520	97
IRAS 22491 − 1808	≥27	≥68000	12

Note. Outflow properties: (1): galaxy name, (2): ratio of kinetic power of the outflow and the bolometric luminosity of the AGN, (3): momentum boost factor, (4): kinetic energy outflow compare to kinetic energy due to SNe.

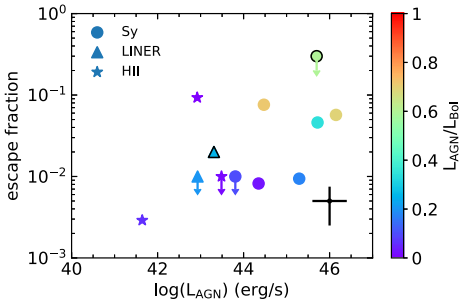

Figure 22. Fraction of the molecular outflow that escapes the galaxy as a function of AGN luminosity. The two data points with a black contour are taken from the literature and use slightly different definitions of escape velocity.

This allows us to compute the escape fractions of gas out of the halo. As expected, we generally obtain escape fractions from the halo even much smaller than the escape fractions from the galaxy, typically much smaller than 1 per cent, further indicating that the bulk of the outflowing gas will remain in the gravitational potential of the system and will eventually re-accrete on to the galaxy. We note, however, that our sample does not include low-mass galaxies ($M_\star < 10^{10}$~M$_\odot$), for which models expect a large fraction of the outflowing gas to leave the galaxy and its halo, hence enriching the IGM. Detailed observations targeting this class of galaxies are needed in order to test these expectations.

4.5 Effectiveness of AGN-driven outflows in quenching star formation

AGN-driven outflows have been claimed to be one of the primary candidates for cleaning galaxies of their gas content hence quenching star formation and transforming them into passive systems. The 'blast-wave' energy-conserving mode, with 100 per cent coupling with the ISM, has generally been regarded as the most effective mode to remove galaxies of their gas content (Zubovas & King 2012). We have, however, obtained various results indicating that such 'ejective' mode is probably not effective in clearing the whole galaxy of its gas content, even at high luminosities. Indeed, most observational properties of the AGN-driven outflows are below the expectations from energy-conserving mode, suggesting either poor coupling efficiency (as suggested by some models and numerical simulations, e.g. Gabor & Bournaud 2014; Costa et al. 2015; Richings & Faucher-Gigùere 2017) or that other driving mechanisms, such as direct radiation pressure on to the ISM dusty clouds, are also at work (Thompson et al. 2015; Costa et al. 2018a; Ishibashi et al. 2018). We have shown that the outflow depletion time-scales for the total gas mass are very long, beyond the typical lifetime of AGN; hence, these outflows are unlikely to expel the whole amount of gas in the galaxy. Finally, as illustrated in the previous section, only a small fraction of the outflowing gas actually escapes the galaxy (and even less the halo); hence, most of the expelled gas re-accretes on the galaxy to fuel star formation.

Although, the AGN 'ejective' mode does not seem capable of quenching the entire galaxy, it can likely clean and quench the central region. Indeed, the outflow depletion time associated with the (mostly centrally concentrated) molecular gas is much shorter ($\sim 10^7$ yr), especially in luminous AGN. Therefore, the ejective AGN mode (especially when occurring at high redshift) may actually be an important route for quenching star formation in the bulge region.

The AGN-driven outflow may also have an additional indirect effect on larger scales. Although the ejective mode is likely confined to the central regions, the energy injected by the outflow into the halo can contribute to keep it hot, hence preventing further gas accretion on to the galaxy and therefore resulting in a 'delayed' quenching, by starvation, once star formation has used up the gas available in the disc (Costa et al. 2015, 2018a). This 'preventive', delayed mode is supported by various statistical properties of the local population of galaxies (Peng, Maiolino & Cochrane 2015; Woo, Son & Bae 2017; Cresci & Maiolino 2018).

5 CONCLUSIONS

In this work, we have quantified the energetics of molecular outflows in a sample of 45 local ($z < 0.2$) galaxies including AGN host galaxies as well as star-forming/starburst galaxies. The sample spans a range in AGN luminosity from $\log(L_{AGN}) \sim 41$ up to $\sim$46 erg s^{-1} and in SFR from $\sim$0.1 up to several 100 M$_\odot$ yr^{-1}. Molecular outflow properties are inferred from interferometric observations of low-J CO lines (apart from four galaxies, for which OH absorption from *Herschel* is used). We collect data of molecular outflows from the literature and recalculate outflow and host galaxy properties in a consistent manner. Furthermore, we also analyse all public ALMA archival data of low-J (1–0, 2–1 and 3–2) CO lines in local galaxies and look for signatures of outflowing gas. This is the largest sample to date for which molecular outflows in CO have been investigated, and includes also less powerful outflows than previous studies. Our sample improves with respect to previous studies not only in terms of statistics but also by reducing the bias favouring very active galaxies that have been preferentially targeted in the past.

Our main findings can be summarized as follows:

(i) For about 30 per cent of the galaxies, we could also obtain information on the ionized outflow, while for 18 per cent of the

sample we have also information on the neutral outflow. We find that in starburst galaxies the ionized outflow is about as massive as the molecular outflow. In AGN, the ionized outflows is generally negligible comparable to the molecular outflow and we find that the molecular-to-ionized outflow rate increases with AGN luminosity. The amount of gas in the atomic neutral phase has a large scatter, but in general is comparable to the molecular phase.

(ii) The molecular mass-loading factor ($\eta = \dot{M}_{\rm outf}({\rm H_2})/{\rm SFR}$) for star-forming galaxies is consistent with unity, as expected by models of star formation feedback.

(iii) The molecular mass-loading factor is higher in AGN host galaxies compared to star-forming galaxies, although a significant boost (with $\eta > 10$) is only seen in galaxies in which the AGN luminosity is high relative to the bolometric luminosity ($L_{\rm AGN}/L_{\rm bol} > 0.7$).

(iv) In AGN, the outflow rate correlates with the AGN luminosity and with the Eddington ratio, $L_{\rm AGN}/L_{\rm Edd}$, although with large scatter, further indicating that the AGN plays a role in driving outflows. We also observe a correlation with the black hole mass, which can be seen as tracing a link between the outflow (which has a dynamical time-scale of 10^6-10^8 yr, much longer than the AGN flickering time-scale) with the integrated, average past activity of the black hole.

(v) We highlight that the dependence of the outflow properties on AGN luminosity, SFR, and galaxy stellar mass makes it difficult to isolate the individual dependences, as each these properties are can be mutually correlated in galaxies. Therefore, we have derived a relation of the outflow rate simultaneously fitting the dependence of AGN luminosity, SFR, and stellar mass. The resulting fit is much tighter than the individual relations and enables us to disentangle, at least partially, the individual dependences. In particular, we obtain a scaling of the outflow rate on stellar mass as $\propto M_\star^{-0.41}$, which is very close to the dependence expected by models of outflows driven by SNe and stellar winds. We also suggest that the inferred empirical (four-dimensional) relation between outflow rate, $L_{\rm AGN}$, SFR, and $M_\star$ can be very efficiently used to predict the strength of outflows in a variety of galaxies and for comparison with models.

(vi) We find that the majority of the molecular outflows studied here show no excess of radio emission relative to the SFR–radio relation. In addition, there is no correlation between molecular outflow rate and IR-to-radio luminosity ratio, indicating that the majority of molecular outflows are not driven by radio jets, at least within the luminosity range probed by us. However, this does not exclude that radio jet may have an important role in driving molecular outflows in a few specific galaxies, as indeed observed.

(vii) The depletion time-scale associated with outflow (i.e. $\tau_{\rm depl} = M_{\rm gas}/\dot{M}_{\rm outf}$) anticorrelates with AGN luminosity, i.e. is shorter in more luminous AGN. The depletion time-scale for molecular gas [$\tau_{\rm depl,outf}({\rm H_2}) = M({\rm H_2})/\dot{M}_{\rm outf}({\rm H_2})$] can be as short as a few, or a few tens million years, much shorter than the depletion time-scale associated with star formation only. However, when considering also the atomic component, the depletion time-scale for the total gas content [$\tau_{\rm depl,outf}({\rm tot}) = M({\rm H_2}+{\rm HI})/\dot{M}_{\rm outf}({\rm H_2})$] is typically of the order, or longer than 10^8 yr, i.e. longer than the typical AGN lifetime. This indicates that the AGN-driven outflow is generally capable of quickly removing the gas from the central regions (which are dominated by the molecular phase), but unlikely to clean the entire galaxy from its gas content.

(viii) For AGN host galaxies, the outflow kinetic power $P_{\rm K,outf}({\rm H_2})$ shows a much larger scatter than in previous studies and spans from 0.1 to 5 per cent of $L_{\rm AGN}$. The ratio $P_{\rm K,outf}({\rm H_2})/L_{\rm AGN}$ increases with luminosity. The momentum rate spans from 1 to 30 times $L_{\rm AGN}/c$. These results suggest that the AGN-driven outflows can be both energy driven (with a broad range of coupling efficiencies with the ISM) and radiation pressure driven.

(ix) We estimate that the fraction of outflowing gas with a high enough velocity to escape the galaxy and the dark matter halo is less than 5 per cent, indicating that, although outflows can remove gas from the central region, most of the gas re-accretes on to the galaxy.

(x) The results on the kinetic power, on the momentum rate, on the depletion time-scale and on the fraction of escaping case, considered all together, indicate that the AGN 'ejective mode' is unlikely to be effective in cleaning the galaxy of its gas content, at least in the mass range probed by us ($> 10^{10}$ M$_\odot$). However, AGN outflows are likely capable of cleaning the gas content, hence quench star formation, in the central (bulge) region. Moreover, AGN-driven outflows can inject energy into the halo hence keeping it hot and preventing further gas accretion, therefore resulting in a delayed feedback that quenches the galaxy through starvation (Peng et al. 2015; Woo et al. 2017).

(xi) In star-forming galaxies, the kinetic power is only 1–2 per cent of the kinetic power generated by SNe, indicating very fast cooling of SN ejecta in the dense ISM in which they explode, hence poor efficiency in driving outflows, as expected by some models. In star-forming galaxies, the momentum rate of outflows correlates with the bolometric luminosity, and it is about 0.3 $L_{\rm bol}/c$, suggesting that radiation pressure can also contribute to drive outflows in star-forming galaxies.

(xii) We also identify about 10 per cent of the galaxies whose outflow significantly exceeds the maximum theoretical values of kinetic power and momentum rate expected for both AGN and SB-driven cases. Our proposed explanation is that these are 'fossil outflows' resulting from activity of a past strong AGN, which has now faded. Theoretical models expects such fossil outflows to be present in large numbers, also simply based on the fact that the outflows dynamical time-scales is of the order of 10^6–10^8 yr, while the AGN has a much shorter variability (1–10^6 yr). Previous outflow surveys have not identified such fossil outflows because they may have been biased towards powerful AGN and powerful starburst galaxies in order to maximize the probability of detecting outflows. Our sample is less biased in this sense (as it includes galaxies that were not selected specifically with the goal of detecting outflows), which has enabled us to detect this phenomenon. However, our sample is still biased, hence the fraction of fossil outflow found by us is probably still the tip of the iceberg of a larger population.

ACKNOWLEDGEMENTS

We thank Fabrizio Fiore and Kastytis Zubovas for their detailed comments on the draft. RM and SC acknowledge support by the Science and Technology Facilities Council (STFC). RM and AF acknowledge ERC Advanced Grant 695671 'QUENCH'. CC acknowledges funding from the European Union's Horizon 2020 research and innovation programme under the Marie Sklodowska-Curie grant agreement no. 664931. ACF and WI acknowledge ERC Advanced Grant 3409442 'FEEDBACK'. MAB acknowledges support by the ERC starting grant 638707 'BHs and their host galaxies: co-evolution across cosmic time'. This paper makes use of the following ALMA data: ADS/JAO.ALMA#2013.1.00659.S, ADS/JAO.ALMA#2012.1.00377.S, ADS/JAO.ALMA#2012.1.00611, ADS/JAO.ALMA#2015.1.00102.S, ADS/JAO.ALMA#2015.1.00263.S, ADS/JAO.ALMA#2013.1.00379.S, ADS/JAO.ALMA# 2012.1.00539, ADS/JAO. ALMA# 2016.1.01279.S. This

research has made use of the NASA/ IPAC Infrared Science Archive, which is operated by the Jet Propulsion Laboratory, California Institute of Technology, under contract with the National Aeronautics and Space Administration. This publication makes use of data products from the Two Micron All Sky Survey, which is a joint project of the University of Massachusetts and the Infrared Processing and Analysis Center/California Institute of Technology, funded by the National Aeronautics and Space Administration and the National Science Foundation.

REFERENCES

Aalto S. et al., 2015, A&A, 574, A85
Aalto S., Muller S., Sakamoto K., Gallagher J., Martín S., Costagliola F., 2012, A&A, 546, A68
Alonso-Herrero A., Engelbracht C. W., Rieke M. J., Rieke G. H., Quillen A. C., 2001, ApJ, 546, 952
Armus L. et al., 2004, ApJS, 154, 178
Arribas S., Colina L., Bellocchi E., Maiolino R., Villar-Martín M., 2014, A&A, 568, A14
Baan W. a., Salzer J. J., LeWinter R. D., 1998, ApJ, 509, 633
Beckmann R. S. et al., 2017, MNRAS, 472, 949
Belfiore F. et al., 2016, MNRAS, 461, 3111
Bellocchi E., Arribas S., Colina L., Miralles-Caballero D., 2013, A&A, 557, A59
Bell E. F., de Jong R. S., 2001, ApJ, 550, 212
Bell E. F., McIntosh D. H., Katz N., Weinberg M. D., 2003, ApJS, 149, 289
Best P. N., Kauffmann G., Heckman T. M., Ivezić Ž., 2005, MNRAS, 362, 9
Bieri R., Dubois Y., Rosdahl J., Wagner A., Silk J., Mamon G. A., 2017, MNRAS, 464, 1854
Bischetti M. et al., 2017, A&A, 598, A122
Bolatto A. D., Wolfire M., Leroy A. K., 2013, ARA&A, 51, 207
Bourne M. A., Nayakshin S., Hobbs A., 2014, MNRAS, 441, 3055
Bourne M. A., Zubovas K., Nayakshin S., 2015, MNRAS, 453, 1829
Brightman M., Nandra K., 2011, MNRAS, 414, 3084
Brusa M. et al., 2018, A&A, 612, A29
Cano-Diaz M. et al., 2012, A&A, 537, L8
Carniani S. et al., 2015, A&A, 580, A102
Carniani S. et al., 2016, A&A, 591, A28
Carniani S. et al., 2017, A&A, 605, A105
Cazzoli S., Arribas S., Maiolino R., Colina L., 2016, A&A, 590, A125
Chisholm J., Tremonti C. A., Leitherer C., Chen Y., 2017, MNRAS, 469, 4831
Cicone C. et al., 2014, A&A, 562, A21
Cicone C. et al., 2015, A&A, 574, A14
Cicone C. et al., 2018b, ApJ, 863, 143
Cicone C., Feruglio C., Maiolino R., Fiore F., Piconcelli E., Menci N., Aussel H., Sturm E., 2012, A&A, 543, A99
Cicone C., Brusa M., Ramos Almeida C., Cresci G., Husemann B., Mainieri V., 2018a, Nat. Astron., 2, 176
Combes F. et al., 2013, A&A, 558, A124
Costa T., Sijacki D., Haehnelt M. G., 2014, MNRAS, 444, 2355
Costa T., Sijacki D., Haehnelt M. G., 2015, MNRAS, 448, L30
Costa T., Rosdahl J., Sijacki D., Haehnelt M., 2018a, MNRAS, 479, 2079
Costa T., Rosdahl J., Sijacki D., Haehnelt M. G., 2018b, MNRAS, 473, 4197
Cresci G. et al., 2015, A&A, 582, A63
Cresci G., Maiolino R., 2018, Nat. Astron., 2, 179
Dasyra K. M., Combes F., Novak G. S., Bremer M., Spinoglio L., Pereira Santaella M., Salomé P., Falgarone E., 2014, A&A, 565, A46
Dasyra K. M., Bostrom A. C., Combes F., Vlahakis N., 2015, ApJ, 815
Dasyra K. M., Combes F., Oosterloo T., Oonk J. B. R., Morganti R., Salomé P., Vlahakis N., 2016, A&A, 595, L7
Davé R., Oppenheimer B. D., Finlator K., 2011, MNRAS, 415, 11
Duc P.-A., Mirabel I. F., Maza J., 1997, A&AS, 124, 533
Duffy A. R., Schaye J., Kay S. T., Vecchia C. D., 2008, MNRAS, 390, L 1
Erb D. K., 2015, Nature, 523, 169
Fabian A., 2012, ARA&A, 50, 455
Fabian A. C., Vasudevan R. V., Gandhi P., 2008, MNRAS, 385,
Faucher-Giguere C. A., Quataert E., 2012, MNRAS, 425, 605
Feruglio C. et al., 2015, A&A, 583, A99
Feruglio C. et al., 2017, A&A, 608, A30
Feruglio C., Maiolino R., Piconcelli E., Menci N., Aussel H., Lamastra A., Fiore F., 2010, A&A, 518, L155
Finlator K., Davé R., 2008, MNRAS, 385, 2181
Fiore F. et al., 2017, A&A, 601, A143
Fischer J. et al., 2010, A&A, 518, L41
Franceschini A. et al., 2003, MNRAS, 343, 1181
Gabor J. M., Bournaud F., 2014, MNRAS, 441, 1615
Gallerani S., Pallottini A., Feruglio C., Ferrara A., Maiolino R., Vallini L., Riechers D. A., Pavesi R., 2018, MNRAS, 473, 1909
García-Burillo S. et al., 2015, A&A, 580, A35
Gil de Paz A. et al., 2007, ApJS, 173, 185
Gilli R., Maiolino R., Marconi A., Risaliti G., Dadina M., Weaver K. A., Colbert E. J. M., 2000, A&A, 355, 485
Gilli R., Calura F., D'Ercole A., Norman C., 2017, A&A, 603, A69
González-Alfonso E. et al., 2017, ApJ, 836, 11
González-Martín O., Masegosa J., Márquez I., Guainazzi M., Jiménez-Bailón E., 2009, A&A, 506, 1107
Greene J. E., Zakamska N. L., Smith P. S., 2012, ApJ, 746, 86
Harrison C. M., Alexander D. M., Mullaney J. R., Swinbank A. M., 2014, MNRAS, 441, 3306
Heckman T. M., Kauffmann G., Brinchmann J., Tremonti C., White S. D. M., Charlot S., Tremonti C., White S. D. M., 2004, ApJ, 613, 109
Heckman T. M., Alexandroff R. M., Borthakur S., Overzier R., Leitherer C., 2015, ApJ, 809
Hernquist L., 1990, ApJ, 356, 359
Ho L., Filippenko A., Sargent W., 1993, ApJ, 417, 63
Ho L. C., Filippenko A. V., Sargent W. L. W., 1997, ApJS, 112, 315
Ishibashi W., Fabian A. C., 2015, MNRAS, 451, 93
Ishibashi W., Banerji M., Fabian A. C., 2017, MNRAS, 469, 1496
Ishibashi W., Fabian A. C., Maiolino R., 2018, MNRAS, p. sty236
Ivison R. J. et al., 2010, MNRAS, 402, 245
Janssen A. et al., 2016, ApJ, 822, 43
Kelly B. C., 2007, ApJ, 665, 1489
Kennicutt R. C., 1998, ApJ, 498, 541
Kennicutt R. C., Evans N. J., 2012, ARA&A, 50, 531
Kewley L. J., Groves B., Kauffmann G., Heckman T., 2006, MNRAS, 372, 961
King A., Nixon C., 2015, MNRAS, 453, L46
King A., Pounds K., 2015, ARA&A, 53, 115
King A. R., 2010, MNRAS, 402, 1516
King A. R., Zubovas K., Power C., 2011, MNRAS, 415, L6
LaMassa S. M., Heckman T. M., Ptak A., Martins L., Wild V., Sonnentrucker P., Hornschemeier A., 2011, ApJ, 729, 52
Lena D. et al., 2015, ApJ, 806, 84
Leroy A. K., Walter F., Decarli R., Bolatto A., Zschaechner L., Weiss A., 2015, ApJ, 811, 15
Lutz D., Maiolino R., Spoon H. W. W., Moorwood A. F. M., 2004, A&A, 418, 465
Maiolino R. et al., 2012, MNRAS, 425, L66
Maiolino R., Rieke G., 1995, ApJ, 454, 95
Mannucci F., Pozzetti L., Thompson D., Oliva E., Baffa C., Comoretto G., Gennari S., Lisi F., 2002, MNRAS, 329, 57
Marconi A., Risaliti G., Gilli R., Hunt L. K., Maiolino R., Salvati M., 2004, MNRAS, 351, 169
McIntosh D. H. et al., 2005, ApJ, 632, 191
McMullin J. P., Waters B., Schiebel D., Young W., Golap K., 2007, in Shaw R. A., Frank H., Bell D. J., eds, ASP Conf. Ser. Vol. 376 Astronomical Data Analysis Software and Systems XVI. Astron. Soc. Pac, San Francisco, p. 127
Miller C. J., Nichol R. C., Gomez P. L., Hopkins A. M., Bernardi M., 2003, ApJ, 597, 142
Mitra S., Davé R., Finlator K., 2015, MNRAS, 452, 1184
Monreal-Ibero A., Arribas S., Colina L., 2006, ApJ, 637, 138

Morganti R., Tadhunter C. N., Oosterloo T. A., 2005, A&A, 444, L9
Morganti R., Fogasy J., Paragi Z., Oosterloo T., Orienti M., 2013, Science, 341, 1082
Morganti R., Oosterloo T., Raymond Oonk J. B., Frieswijk W., Tadhunter C., 2015, A&A, 580, A1
Morganti R., Veilleux S., Oosterloo T., Teng S. H., Rupke D., 2016, A&A, 593, A30
Moster B. P., Naab T., White S. D. M., 2013, MNRAS, 428, 3121
Mullaney J. R., Alexander D. M., Fine S., Goulding A. D., Harrison C. M., Hickox R. C., 2013, MNRAS, 433, 622
Nardini E., Risaliti G., Salvati M., Sani E., Imanishi M., Marconi A., Maiolino R., 2008, MNRAS, 385, L130
Nardini E., Risaliti G., Salvati M., Sani E., Watabe Y., Marconi A., Maiolino R., 2009, MNRAS, 399, 1373
Nardini E., Risaliti G., Watabe Y., Salvati M., Sani E., 2010, MNRAS, 405, 2505
Navarro J. F., Frenk C. S., White S. D. M., 1995, ApJ, 462, 563
Neff S., Hutchings J., Standord S., Unger S., 1990, AJ, 99, 1088
Peng Y., Maiolino R., Cochrane R., 2015, Nature, 521, 192
Pereira-Santaella M. et al., 2011, A&A, 535, 93
Pereira-Santaella M. et al., 2016, A&A, 594, A81
Perna M. et al., 2015, A&A, 574, A82
Piconcelli E., Jimenez-Bailon E., Guainazzi M., Schartel N., Rodriguez-Pascual P. M., Santos-Lleo M., 2005, A&A, 432, 15
Pineda J. L., Langer W. D., Goldsmith P. F., 2014, A&A, 570, A121
Prieto M. A., Reunanen J., Tristram K. R. W., Neumayer N., Fernandez-Ontiveros J. A., Orienti M., Meisenheimer K., 2010, MNRAS, 402, 724
Puchwein E., Springel V., 2013, MNRAS, 428, 2966
Querejeta M. et al., 2016, A&A, 593, A118
Ricci C. et al., 2017, Nature, 549, 488
Richings A. J., Faucher-Gigùere C.-A., 2017, MNRAS, 000, 1
Richings A. J., Faucher-Giguère C. A., 2018, MNRAS, 474, 3673
Risaliti G., Maiolino R., Salvati M., 1999, ApJ, 522, 157
Roos O., Juneau S., Bournaud F., Gabor J. M., 2015, ApJ, 800
Rupke D. S. N., Gültekin K., Veilleux S., 2017, ApJ, 850, 40
Rupke D. S., Veilleux S., 2013, ApJ, 768
Rupke D. S., Veilleux S., Sanders D. B., 2005a, ApJ
Rupke D. S., Veilleux S., Sanders D. B., 2005b, ApJS, 160, 115
Sakamoto K., Aalto S., Combes F., Evans A., Peck A., 2014, ApJ, 797, 90
Salak D., Nakai N., Hatakeyama T., Miyamoto Y., 2016, ApJ, 823, 68
Sarzi M. et al., 2010, MNRAS, 402, 2187
Scannapieco E., Oh S. P., 2004, ApJ, 608, 62
Schawinski K., Koss M., Berney S., Sartori L. F., 2015, MNRAS, 451, 2517
Severgnini P., Maiolino R., Salvati M., 2000, A&A
Sijacki D., Springel V., Di Matteo T., Hernquist L., 2007, MNRAS, 380, 877
Skrutskie M. F. et al., 2006, AJ, 131, 1163
Solomon P., Vanden Bout P., 2005, ARA&A, 43, 677
Somerville R. S., Davé R., 2015, ARA&A, 53, 51
Spoon H. W. W. et al., 2013, ApJ, 775, 127
Springel V., di Matteo T., Hernquist L., 2005, MNRAS, 361, 776
Stone M., Veilleux S., Meléndez M., Sturm E., Graciá-Carpio J., González-Alfonso E., 2016, ApJ, 826, 111
Strickland D. K., 2007, MNRAS, 376, 523
Sturm E., 2011, ApJ, 733, L16
Sun A.-L., Greene J. E., Zakamska N. L., Nesvadba N. P. H., 2014, ApJ, 790, 160
Takeuchi T. T., Buat V., Iglesias-Páramo J., Boselli A., Burgarella D., 2005, A&A, 432, 423
Taylor E. N. et al., 2011, MNRAS, 418, 1587
Teng S. H. et al., 2009, ApJ, 701, 2035
Teng S. H. et al., 2015, ApJ, 814, 56
Thompson T. A., Quataert E., Murray N., 2005, ApJ, 630, 167
Thompson T. A., Fabian A. C., Quataert E., Murray N., 2015, MNRAS, 449, 147
Toba Y., Komugi S., Nagao T., Yamashita T., Wang W.-H., Imanishi M., Sun A.-L., 2017, ApJ, 851, 98
Tombesi F., Meléndez M., Veilleux S., Reeves J. N., González-Alfonso E., Reynolds C. S., 2015, Nature, 519, 436
Veilleux S. et al., 2009, ApJS, 182, 628
Veilleux S. et al., 2013, ApJ, 776, 27
Veilleux S., Kim D.-C., Sanders D. B., Mazzarella J. M., Soifer B. T., 1995, ApJS, 98, 171
Veilleux S., Kim D., Sanders D. B., 2002, ApJS, 143, 315
Veilleux S., Cecil G., Bland-Hawthorn J., 2005, ARA&A, 43, 769
Veilleux S., Bolatto A., Tombesi F., Meléndez M., Sturm E., González-Alfonso E., Fischer J., Rupke D. S. N., 2017, ApJ, 843, 18
Véron-Cetty M.-P., Véron P., 2010, A&A, 518, A10
Vogelsberger M. et al., 2014, MNRAS, 444, 1518
Walch S., Naab T., 2015, MNRAS, 451, 2757
Walter F. et al., 2017, ApJ, 835, 265
Weiß A., Walter F., Scoville N. Z., 2005, Astron. Astrophys., 438, 533
Westmoquette M. S., Clements D. L., Bendo G. J., Khan S. A., 2012, MNRAS, 424, 416
Woo J.-H. et al., 2010, ApJ, 716, 269
Woo J.-H., Son D., Bae H.-J., 2017, ApJ, 839, 120
Yuan T.-T., Kewley L. J., Sanders D. B., 2010, ApJ, 709, 884
Yun M. S., Reddy N. A., Condon J. J., 2001, ApJ, 554, 803
Zhang Z., Shi Y., Rieke G. H., Xia X., Wang Y., Sun B., Wan L., 2016, ApJ, 819, L27
Zschaechner L. K. et al., 2016, ApJ, 832, 142
Zubovas K., 2015, MNRAS, 451, 3627
Zubovas K., King A., 2012, ApJ, 745, L34

APPENDIX A: A'LMA ARCHIVAL DATA

In Figs A2–A7 of this appendix, we show the ALMA archival data of galaxies in which we have found evidence for outflows. Each figure shows on the top panels the integrated spectrum along with a zoom in the *Y*-axis, and where the blue dashed line shows the narrow component and the red dashed line the broad component tracing the outflow. The central panel shows the position–velocity diagram along the major axis (left) and along the minor axis (right). The bottom panels show the map of the broad wings, i.e. the flux integrated in the velocity ranges where the broad component is stronger than the narrow component (specific velocity ranges are indicated on top of each panel).

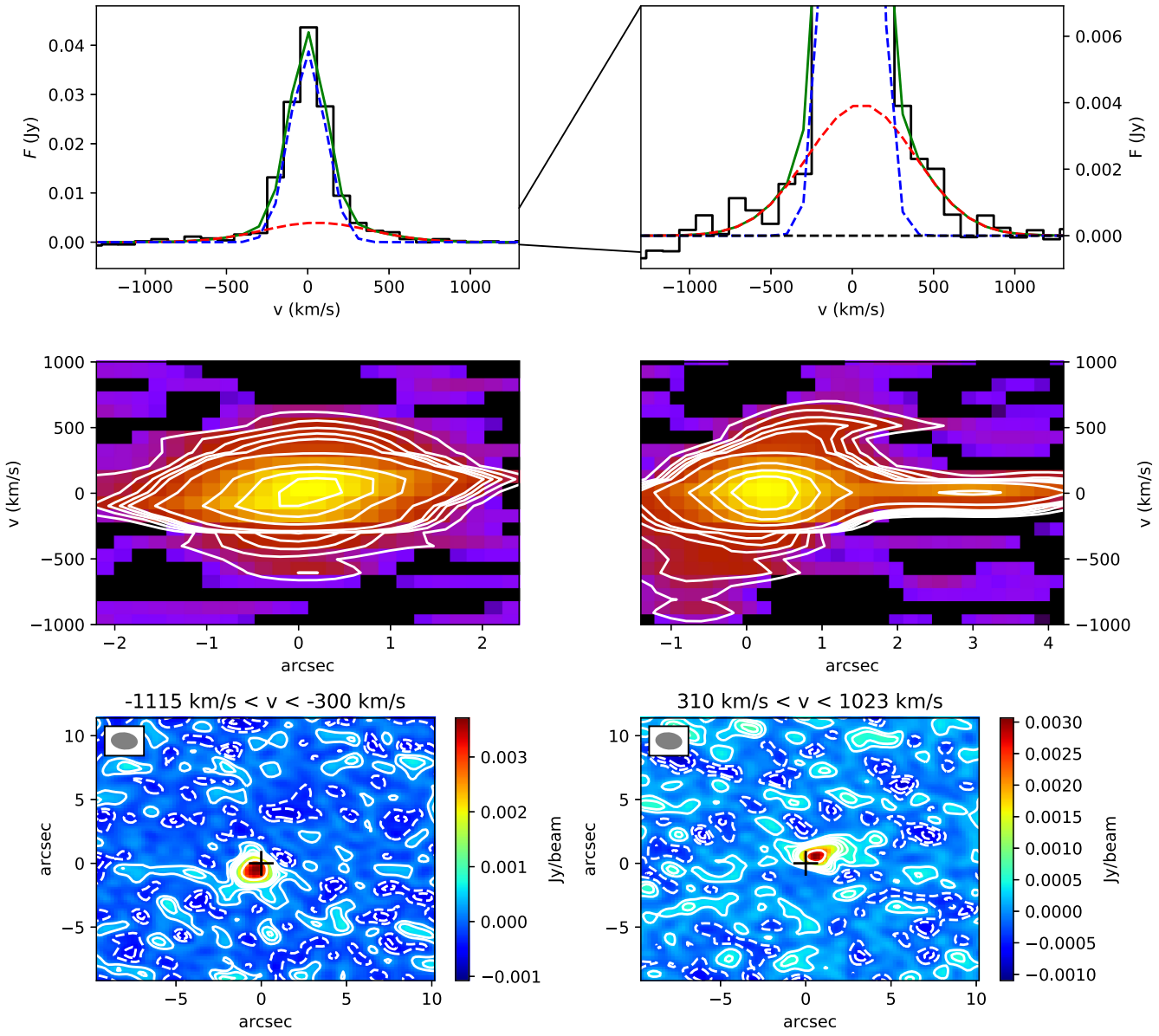

Figure A1. IRAS 20100 − 4156: the top panels show the CO line emission and the fit to the line, where the blue dashed line represents the narrow emission and the red dashed line is the broad component. The two middle panels show the position–velocity diagrams along the major (left) and minor (right) axis with (1, 2, 3, 4, 5, 10, 30, 50, 70)σ contours as white lines. In the bottom panel, the line maps of the wings are depicted (produced by integrating over the spectral range where the broad component, i.e. outflow component, is dominant). The black cross indicates the peak of the narrow emission. Positive contours are shown as white lines (1, 2, 3, 4, 5, 10)σ and negative contour are represented by white dashed lines $(-1, -2, -3)\sigma$.

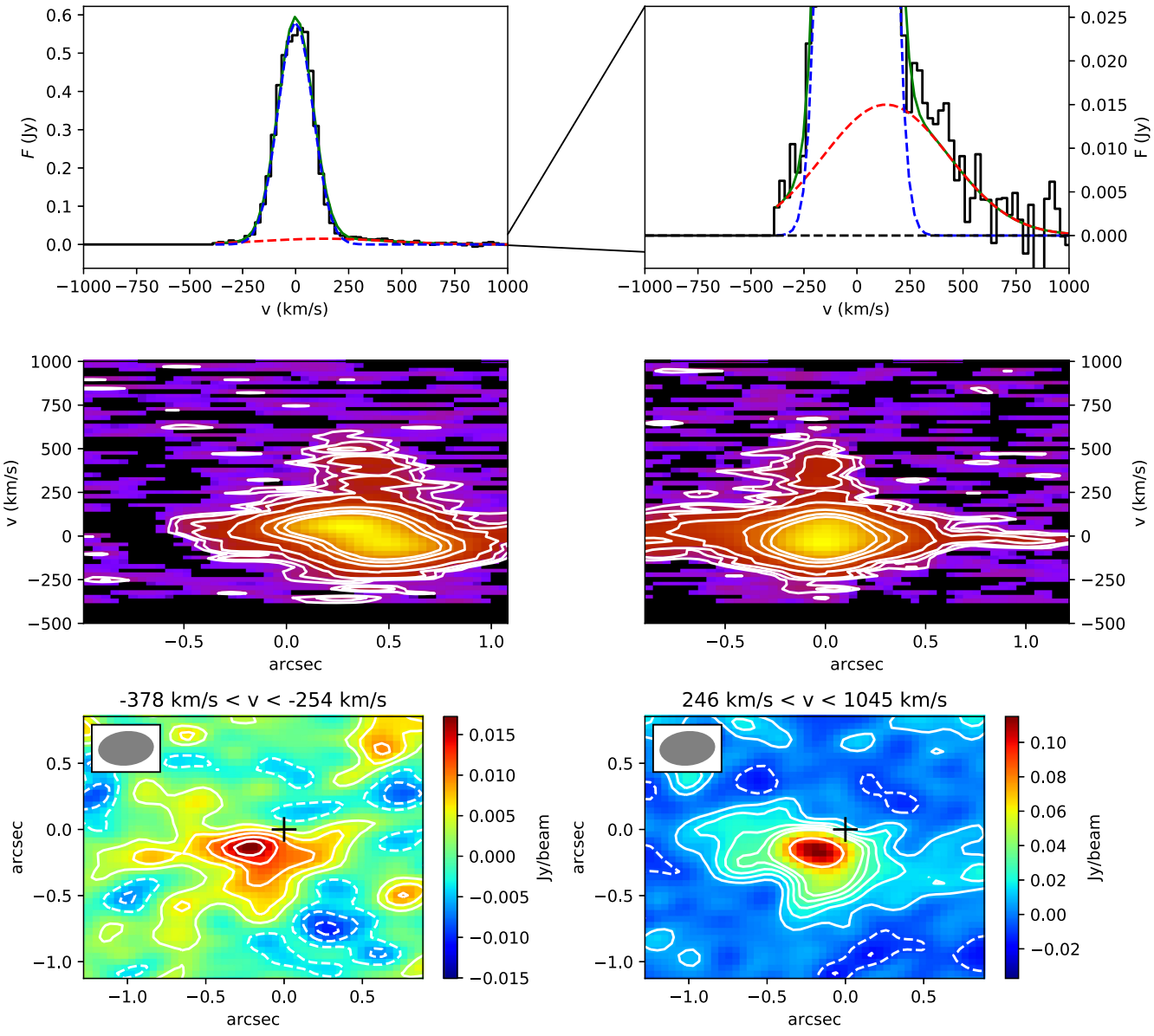

Figure A2. IRAS 05189 − 2524: see caption of Fig. A1, but contours in p–v diagrams (middle panel) are (2, 3, 5, 10, 30, 50, 70)σ.

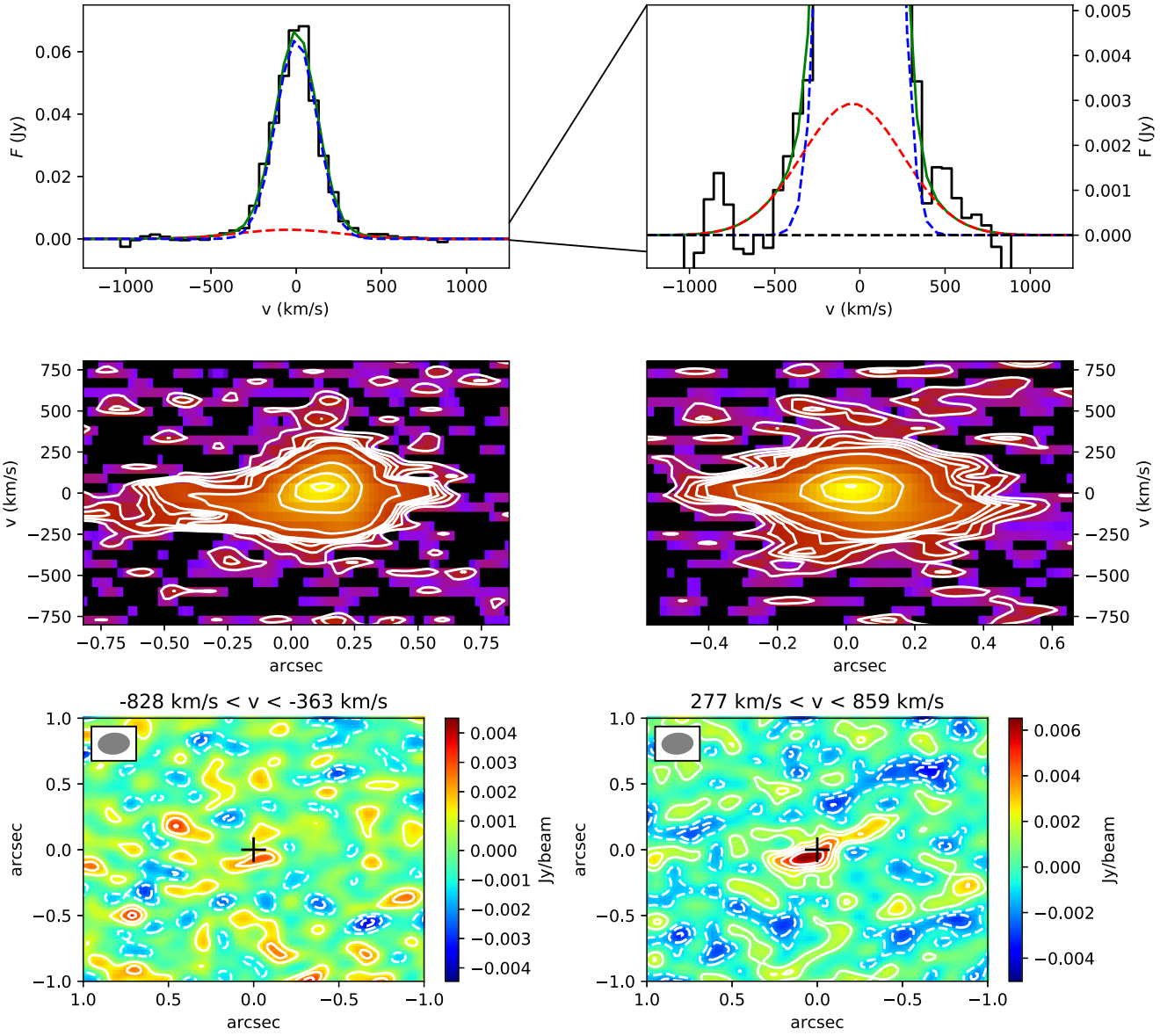

Figure A3. PG 0157 + 001: see caption of Fig. A1.

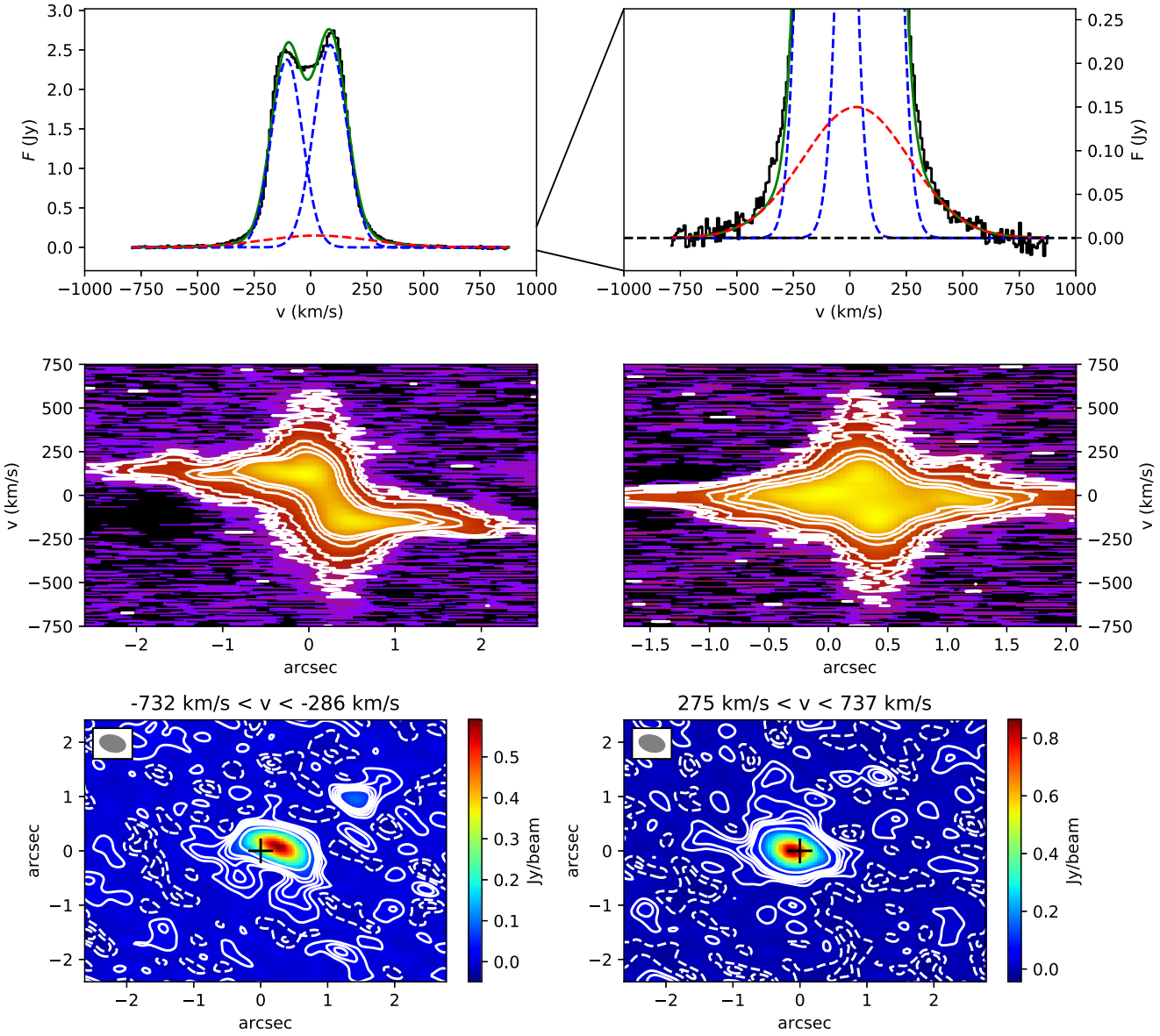

Figure A4. IRAS13120 − 5453: see caption of Fig. A1, but contours in p–v diagrams (middle panel) are (3, 5, 10, 30, 50, 70)σ.

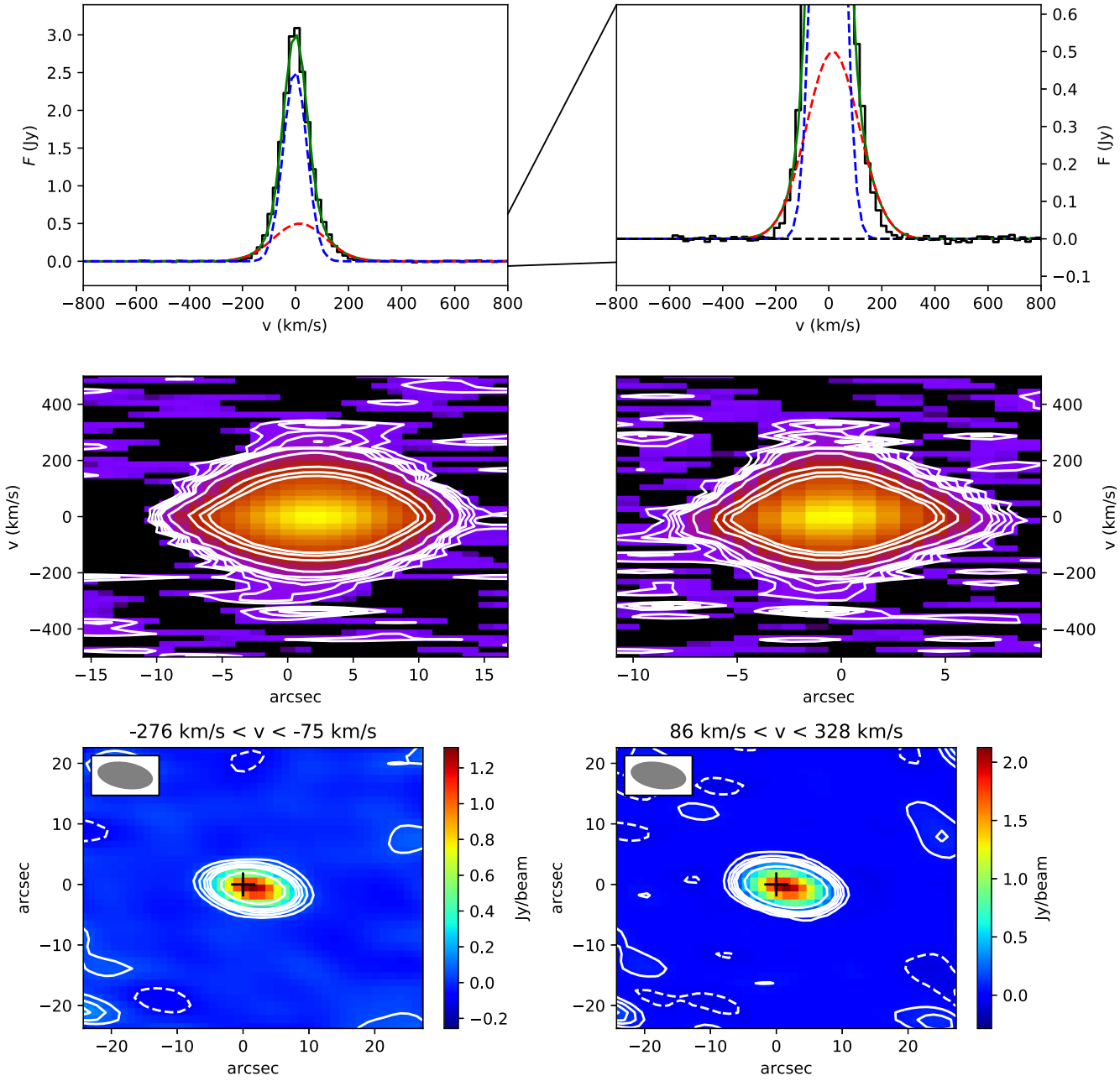

Figure A5. NGC 4418: see caption of Fig. A1.

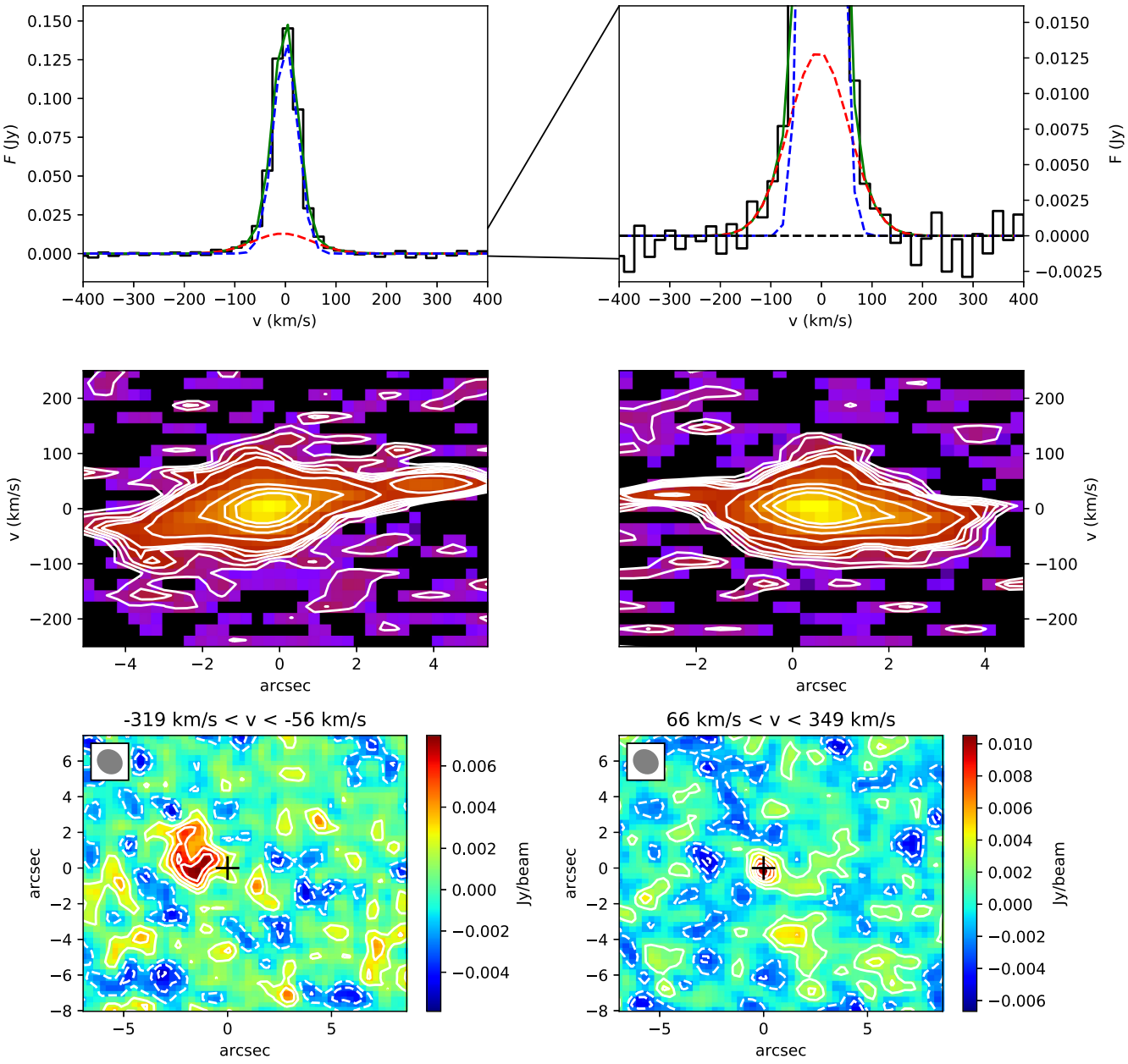

Figure A6. IRAS15515 + 0208: see caption of Fig. A1.

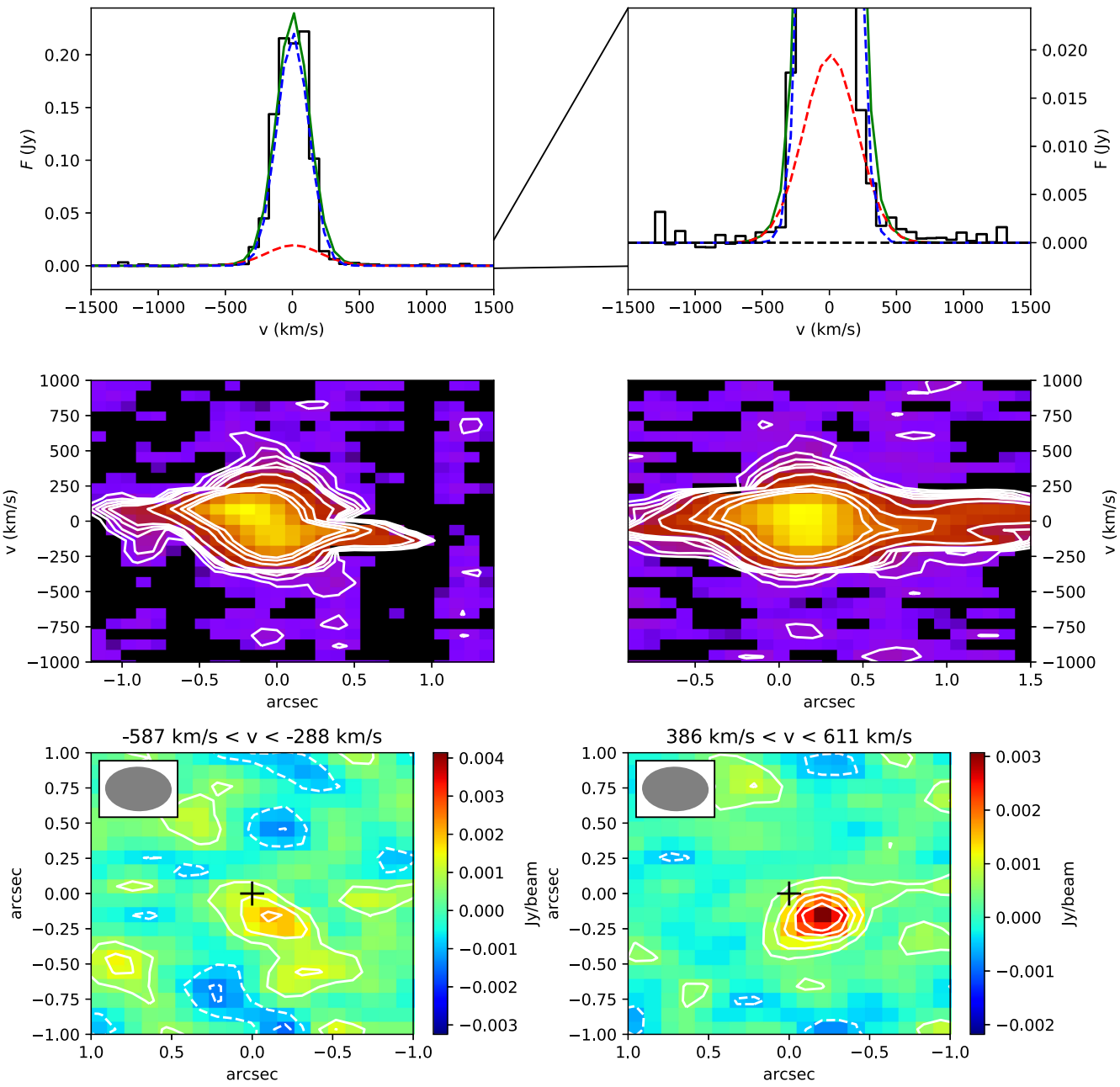

Figure A7. IRAS 22491 − 1808: see caption of Fig. A1.

This paper has been typeset from a TEX/LATEX file prepared by the author.